Preprint

Efficient prediction of broadband trailing edge noise and application to porous edge treatment

Benjamin W. Faßmann Christof Rautmann Roland Ewert
Jan W. Delfs

Institute of Aerodynamics and Flow Technology, Technical Acoustics
German Aerospace Center (DLR)
Lilienthalplatz 7, 381208 Braunschweig, Germany

Trailing edge noise generated by turbulent flow traveling past an edge of an airfoil represents one of the most essential paradigms of aeroacoustic sound generation at solid surfaces. It is of great interest for noise problems in various areas of industrial application. First principle based Computational Aeroacoustics (CAA) methods with short response time are needed in the industrial design process for reliable prediction of spectral differences in turbulent-boundary-layer trailing-edge noise (TBL-TEN) due to design modifications. In this work an aeroacoustic method is studied that rests on a hybrid two-step CFD/CAA procedure. In a first step Reynolds Averaged Navier-Stokes simulation provides the time-averaged solution to the turbulent flow, including the mean-flow and turbulence statistics such as length-scale, time-scale and turbulence kinetic energy. Fluctuating sound sources are stochastically generated from RANS statistics with the Fast Random Particle-Mesh Method (FRPM) to simulate in a second CAA step broadband aeroacoustic sound. From experimental findings it is well known that porous trailing edges significantly lower trailing edge noise level over a large bandwidth of frequencies reaching 6 to 8dB reduction. Furthermore, sound reduction depends on the porous material parameters, e.g. geometry, porosity, permeability and pore size. This paper presents first results for the extended hybrid CFD/CAA method to include the effect on noise of porous materials with specifically prescribed parameters. To incorporate the effect of porosity, an extended formulation of the Acoustic Perturbation Equations (APE) with source terms is derived based on a reformulation of the volume averaged Navier-Stokes equations into perturbation form. Proper implementation of the Darcy and Forchheimer terms is verified for sound propagation in homogeneous and anisotropic porous medium. Sound generation is studied for a generic symmetric NACA0012 airfoil without lift to separate secondary effects of lift and camber on sound from those of the basic edge noise treatments. The reference solid airfoil configurations are compared with published experimental data. Convincing agreement in the prediction of one-third-octave band spectra is found. Simulation with porous edge treatment reveals a broadband noise reduction capability of approximately 6dB with similar trends as seen in experiment.

1. INTRODUCTION

Airfoil self-noise radiated from an airfoil exposed to a flow is caused by different source mechanisms (see Brooks et al. [5]), e.g., vortical structures in a turbulent flow interacting with surfaces, see Howe [33, Ch. 6, 7] or Wagner et al. [50]. Turbulent-boundary-layer trailing-edge noise (TBL-TEN) represents one of the most prominent source mechanisms that is important for a wide range of technical applications like noise generated at the airframe of an aircraft with the high-lift system deployed, broadband fan noise generated in turbo machines, or noise generated by the turbulent flow at wind turbine rotor blades.

Over the last two decades the renewable energy share in the global energy mix has grown steadily. Among different sources the wind power sector has made significant progress. The maturation of the technology together with constant installation of new turbines have pushed the cumulative installed capacity to 282.5 GW worldwide at the end of 2012. That represents an average annual growth rate in worldwide wind energy capacity of 22 % over the last 10 years, see GWEC [20]. In its market forecast the Global Wind Energy Council (GWEC) predicts a cumulative installed capacity of about 500 GW at the end of 2017. This process goes hand in hand with the construction of new wind farms and the replacement of older turbines with newer more efficient ones (repowering). Basically, two points are important in the development of new wind farms: annual energy production (AEP) of the turbines and the size and location of the wind farm. To achieve a high AEP, rotor diameters are increasing up to the structural limits resulting in rotor blade lengths of up to 70 m. Turbine size becomes an even more important parameter at locations with low average wind speeds where the total amount of kinetic energy in the wind is low and therefore a bigger rotor cross sectional area is needed to harvest as much energy as possible, refer to Hau [23, Ch. 14, 19, 20]. Due to the shortage of new on-shore building cites wind farms are moving closer to residential areas. Besides the anesthetic circumstances noise immissions are one major issue for nearby living people.

The efficient and reliable prediction of wind turbine noise in the development process of a new turbine is crucial for quiet rotor blade design (see Schepers et al. [43]). As a first step towards establishing an aeroacoustic design capability one could think of evaluating the aeroacoustic properties of different rotor blade shapes already in the aerodynamic design phase. After the basic shape is determined, supplementary trailing-edge modification can be applied to achieve an even greater reduction of noise emission. Hence, the prediction-method should also be capable of calculating the noise reduction effect of trailing edge treatments based on porous materials.

For trailing-edge noise different prediction approaches are known ranging from fast and simple semi-empirical methods like the Brooks, Pope and Marcolini (BPM) model (see Brooks et al. [5]) to high fidelity scale resolving numerical simulation methods like Large Eddy Simulation (LES). As the semi empirical method is based on reference measurements, it is prone to inaccuracy when applied to airfoils which significantly deviate from the reference geometry. Furthermore, it can only be used for 2-D calculations, thus no 3-D modification of the trailing edge (e.g. serrations) can aeroacoustically be evaluated. Alternatively, one could use more sophisticated 3-D time and space resolved LES simulation. Significant for this approach is still its very high computational effort.

In the field of aircraft application, future prospective of short range aircraft with short take off and landing (STOL) properties involve non-conventional high lift systems as overblown flaps taking advantage of the coanda effect, see Radespiel and Heinze [41]. In this context, additional sound generation must be avoided, at first place. In 1979, Hayden [24] investigated several edge concepts for overblown flaps. Howe [32] presented a basic theory on this. Besides simple trailing-edge modifications, the application of porous material is another promising means for reducing trailing edge noise, see Hayden and Chanaud [25]. The positive effect of lengthwise slits applied to the trailing edge was shown by Herr [26]. The resulting reduction compared to the solid reference is about 6 dB. As the manufacturing of narrow slits is expensive it is of crucial interest to investigate the acoustic benefit of rigid porous material as sintered metal fiber felts or metal foams. A variety of porous materials applied to the trailing edge of a high lift airfoil is tested by Herr et al. [29]. Maximal sound reduction of about 6 dB to 8 dB is reported.

Prospective noise optimization in all fields should be integrated into the airfoil design process to enable short-term development cycles aspired by the industry. Today's computational power allows a detailed and high resolution investigation of a variety of approaches to conquer the edge noise problem. But full resolution of porous material with all its geometrical details at technical relevant Reynolds numbers still exceeds datum computer capability. Thus, a frequently used means of modeling porous material and multi-phase flow is the method of volume averaging, refer to Bear and Corapcioglu [2], Drew [9], Gray [18], Gray and Lee [19], Hassanizadeh and Gray [21], Hassanizadeh [22], Ni and Beckermann [38], Slattery [46], Whitaker [51]. Breugem and Boersma [4] uses the Volume Averaged Navier-Stokes (VANS) equations for hydrodynamic applications.

In this article an efficient method with prospective aeroacoustics design quality is applied that utilizes a hybrid two-step CFD/CAA procedure with stochastically realized 4-D spatio-temporal turbulence. In a first step Reynolds Averaged Navier-Stokes simulation provides the time-averaged solution to the turbulent flow, including the mean-flow and turbulence statistics such as length- and time-scales and turbulence kinetic energy. With the Fast Random Particle-Mesh Method (FRPM) fluctuating sound sources are stochastically generated from RANS statistics to simulate in a second CAA step broadband aeroacoustic sound with Acoustic Perturbation Equations (APE) (see Ewert and Schröder [13]). The method has the capability to simulate airfoils of arbitrary geometries and variable flow regime.

The present article aims at extending the application of the hybrid CFD/CAA approach to include the effect of porous trailing-edge modification on broadband sound. Section 2 gives an overview about the applied method and presents the main details of an extended APE reformulation from volume averaging of the Navier-Stokes equations to incorporate the effect of porous medium into CAA simulation. In Section 3, the computational set-up for CFD and CAA simulation is introduced, focusing on resolution constraints. Also a close look on the special issues regarding porous inlays is taken. Section 4 discusses the latest results for the prediction of broadband sound from a generic NACA0012 airfoil with solid trailing edge and its reliability is studied by comparison with experimental results. Further, CAA results for simulation with porous medium are presented. First, generic test cases for the propagation of acoustic waves in homogeneous porous material with spatially isotropic porosity properties on the one hand and spatially anisotropic porosity properties on the other hand are used to verify the implementation. Next, results for

the NACA0012 airfoil with porous trailing edge treatment and stochastic sound sources are compared to the reference case without edge treatment. Finally, main conclusions are drawn in Section 5.

In the paper, only 2-D results are shown. But, for achieving the goal of predicting local 3-D modification of the rotor blade, the presented hybrid approach is performing in 3-D as well. The actual expenses directly depend on the level of detail what should be achieved. If the computations include an elaborate geometry or turbulent structures should be resolved, the computation takes longer than the investigation of some roughly assembled 2-D sections of a well known rotor blade. Beside this adjustment capability of the spatial resolution of the set-up, the implementation of the presented approach is fully parallelized to gain a speed up of the simulations. In addition, the sound field on a collecting surface in the near farfield of the rotor blade can be propagated to an arbitrary observer's position. Using Fast Multipole Boundary Element Method, the sourface pressure can serve as input to calculate the acoustic at a far field position.

2. NUMERICAL METHODS

In this chapter, the numerical methods will be presented which were used for prediction of trailing edge noise at standard and low noise trailing edges. First, the hybrid approach of sequential aerodynamic and aeroacoustic simulations is generally depicted. Second, volume averaged perturbation equations are derived. They will be applied for predicting the edge noise at the porous trailing edge. Finally, the utilized source model for trailing edge noise is specified in detail.

2.1. Hybrid CFD/CAA approach

The approach pursued by DLR relies on a hybrid two-step procedure for a first-principle based prediction of broadband trailing-edge noise. The first step rests on a Computational Fluid Dynamics (CFD) simulation of the time-averaged turbulent flow around the airfoil. In the second Computational Aeroacoustics (CAA) step time dependent linear equations are solved on structured multi-block (SMB) meshes. For the preparation of unsteady vortex sound sources a synthetic turbulence method developed at DLR is adopted to force acoustic perturbation equations. The stochastic approach is especially well suited for aeroacoustics purposes, i.e. realizing a '4-D' time-space based prediction of fluctuating sources in a restricted volume (denominated subsequently as 'source patch') and including the convection of synthetic eddies with proper imposed time decay. The Random Particle-Mesh Method (RPM) by Ewert and Edmunds [12] allows to synthetically realize time-dependent fluctuations from time-averaged turbulence statistics. It generates Gaussian correlated synthetic turbulence of local integral length scale $\Lambda = c_l/C_\mu\sqrt{k}/\omega$ ($c_l \simeq 0.5$, $C_\mu = 0.09$) and variance proportional to the turbulence kinetic energy distribution, refer to Section 2.3 for further details. A numerical revisited approach (refer to Ewert [11], Ewert et al. [15]), termed Fast Random Particle-Mesh Method (FRPM) was applied for the simulations presented in this article.

Fig. 1 gives a general overview about the approach. The steady time-averaged RANS flow (which by means of Birkhoff's ergodic theorem is equivalent to an ensemble average of the flow) provides the mean-flow over which the time dependent aeroacoustic simulation is conducted. Furthermore, the turbulence statistics provided by RANS are utilized to generate the unsteady vortex sound sources that drive the governing equations.

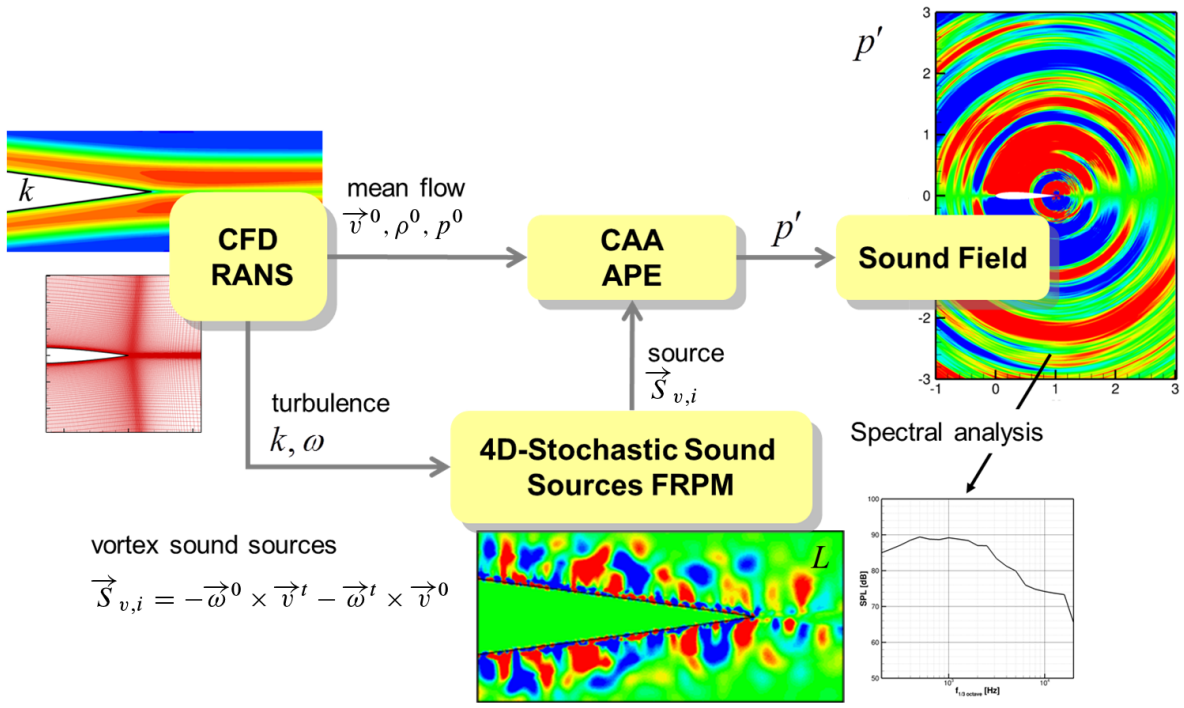

Figure 1: Schematic of CAA prediction method of DLR based on a two-step hybrid method using a steady RANS CFD step, followed by a CAA step solving Acoustic Perturbation Equations (APE) on structured multi block (SMB) meshes; the generation of fluctuating turbulent sound sources is realized with the 4-D FRPM synthetic turbulence method.

In free field this turbulence is coupled with the CAA solver PIANO of DLR (refer to Delfs et al. [7]), which is based on the 4th order accurate DRP scheme proposed by Tam and Webb [47]. The synthetic turbulence in conjunction with the RANS mean-flow defines the right-hand side fluctuating source terms of the Acoustic Perturbation Equations (APE) by Ewert and Schröder [13], which are a modification of the Linearized Euler Equations (LEE) so that vorticity or entropy convection is entirely prescribed by the source term whereas acoustic generation and radiation is simulated dynamically. The APE realize a solution to the wave operator of irrotational flow. Together with proper right-hand side volume sources this becomes an acoustic analogy based on that wave operator. The source term mainly acts as a vorticity production term. Sound due to the interaction of vorticity with the trailing-edge is generated as part of the CAA simulation step. These vortex dynamics are dominated by the linear contributions to the source terms. Non-linear contributions to the source term (self noise term) mainly deemed responsible for sound generation of free turbulent flow are neglected. This is due to the short characteristic time scale related to vorticity passing by the trailing edge in comparison to the turbulent decay time scale in the vicinity of the edge.

2.2. Volume averaged perturbation equations

Volume averaging The method of volume averaging is an important tool for multi-phase flows and since the late 60th, a considerable amount of work has been dedicated to the development of volume averaged conservation and transport equations, see e.g. Bear and Corapcioglu [2], Drew [9], Gray [18], Gray and Lee [19], Hassanizadeh and Gray [21], Hassanizadeh [22], Ni and Beckermann [38], Slattery [46], Whitaker [51]. Basically, the averaging operation can be understood as spatial filtering of the flow variables. The superficial volume averaging is defined as follows:

$$\langle\rho\rangle^s(\boldsymbol{x},t) := \frac{\int G(\boldsymbol{x}-\boldsymbol{x}',\Delta)\,\rho^*(\boldsymbol{x}',t)d^3x'}{\int G(\boldsymbol{x}-\boldsymbol{x}',\Delta)\,d^3x'}. \tag{1}$$

In this expression G denotes the spatial filter applied for the volume averaging procedure. The filter is centered at $\boldsymbol{x}$ and has a fixed extension defined by length scale Δ, i.e. it decays to zero for $|\boldsymbol{x}-\boldsymbol{x}'| >> \Delta$. For example, the filter could be chosen to be a Gaussian with standard deviation Δ.

The quantity ρ^* denotes the generalized density variable which is well defined in the entire volume, i.e. in the porous volume as well as in the solid phase of a porous material. It is given by

$$\rho^*(\boldsymbol{x},t) = \rho(\boldsymbol{x},t)H(f(\boldsymbol{x})). \tag{2}$$

Here, H denotes the Heaviside-function and $f(\boldsymbol{x})$ is a function defined to be $f<0$ in the solid

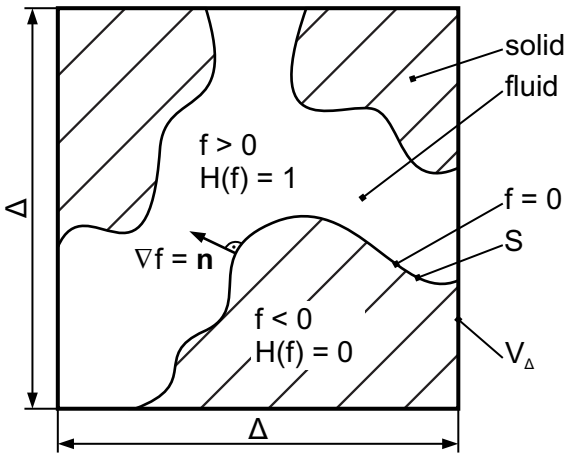

Figure 2: Schematic of porous material and definition of function $f(x)$.

material and $f>0$ in the fluid, i.e. $f=0$ indicates the surface between solid and fluid in the porous medium, refer to Fig. 2. The gradient of $f(0)$ is normal to the interface surfaces. Without losing generality we can define the scaling of f such that the gradient is the wall normal unity vector and points into the fluid, i.e. $\boldsymbol{\nabla} f = \boldsymbol{n}$. For further details regarding generalized variables and their application refer to Crighton et al. [6]. The integrals (without explicitly specified bounds) are taken over the entire space. In general, the integral over the filter kernel defines a characteristic filter volume,

$$V_\Delta = \int G(\boldsymbol{x}-\boldsymbol{x}',\Delta)\,d^3x'. \tag{3}$$

The intrinsic averaged density is defined by

$$\langle\rho\rangle^i(\boldsymbol{x},t) := \frac{\int G(\boldsymbol{x}-\boldsymbol{x}',\Delta)\,\rho^*(\boldsymbol{x}',t)d^3x'}{\int G(\boldsymbol{x}-\boldsymbol{x}',\Delta)\,H(f(\boldsymbol{x}'))d^3x'}. \tag{4}$$

We can define a porosity factor $\bar{\phi}$ via

$$\bar{\phi} = \frac{\int G(\boldsymbol{x}-\boldsymbol{x}',\Delta)\,H(f(\boldsymbol{x}'))d^3x'}{\int G(\boldsymbol{x}-\boldsymbol{x}',\Delta)\,d^3x'}, \tag{5}$$

which, based on the definitions Eqs. (1) and (4) for intrinsic and superficial averaged quantities, yields the following generally valid relationship between both volume averaged quantities:

$$\langle\rho\rangle^s = \bar{\phi}\ \langle\rho\rangle^i. \tag{6}$$

It always is $0 \leq \bar{\phi} \leq 1$, where $\bar{\phi} = 1$ in free fluid and $\bar{\phi} = 0$ represents a solid body.

In the special case where the filter kernel is chosen to be a discontinuous top-hat function $G(\boldsymbol{x}-\boldsymbol{x}',\Delta) = g(x-x')g(y-y')g(z-z')$, where $g(x)$ is defined by

$$g(x) = 1 - H(|x| - \Delta/2), \tag{7}$$

the superficial averaged density reads

$$\langle\rho\rangle^s = \frac{1}{V_\Delta}\int\limits_{V_F}\rho d^3x'. \tag{8}$$

The top-hat function restricts the integration volume to a finite extension $V_\Delta = \Delta^3$ centered at the given position (window averaging). V_F is the fluid volume of the porous material inside the actual window; it satisfies $V_F = \bar{\phi}V$. The intrinsic volume averaged variable in this case becomes

$$\langle\rho\rangle^i = \frac{1}{V_F}\int\limits_{V_F}\rho d^3x'. \tag{9}$$

For a point inside the fluid phase the intrinsic density becomes in the limit $\Delta \to 0$ equal to the local density in the fluid, i.e.

$$\langle\rho\rangle^i(\boldsymbol{x},t) \to \rho(\boldsymbol{x},t) \quad \text{for} \quad \Delta \to 0. \tag{10}$$

In order to smooth out geometrical details of the porous medium, such that the volume averaged variables become continuous over the porous material, a length scale $\Delta > D_p$ must be used, where D_p denotes a length scale derived from a characteristic pore size. In this case, the intrinsic volume averaged density has the same order of magnitude as a local density, it is, however, a quantity defined over the entire space, which moreover can be spatially differentiated if a continuous filter function G is applied. The superficial averaged density is smaller as defined by the porosity parameter $\bar{\phi}$. Hence, at interfaces between porous materials and free fluid the intrinsic density will only exhibit a gradual change over the interface, whereas the superficial averaged density will change rapidly over a scale Δ. Inside a homogeneous porous material, the explicit value of $\bar{\phi}$ will be independent for sufficient large Δ from the explicit chosen length scale in Eq. (5). However, at

an interface between the porous medium and a free fluid, $\bar{\phi}$ will change gradually over a length Δ from its value in the porous medium to one inside the fluid phase.

Favre volume averaged velocities are defined via

$$[v_i] = \frac{\langle \rho v_i \rangle^{s,i}}{\langle \rho \rangle^{s,i}}. \tag{11}$$

As a consequence of definitions Eqs. (1) and (5) the definition is independent as to whether superficial or intrinsic averaging is applied. To derive volume averaged perturbation equations, the Navier-Stokes equations in conservative notation are volume averaged assuming the application of a spatial differentiable filter $G(|\boldsymbol{x}-\boldsymbol{x}'|)$. In the fluid ($\bar{\Phi}=1$) the resulting equations correspond to those used for large eddy simulation (LES), i.e. they formally correspond to the Navier-Stokes equations for volume averaged variables plus some extra subgrid scale stress terms on the right-hand side. In this derivation step, commutation of volume averaging and differentiation is applied, e.g. for the term ρv_i in the continuity equation it follows from the definition Eq. (1)

$$\left\langle \frac{\partial \rho v_i}{\partial x_i} \right\rangle^s = \frac{\partial}{\partial x_i} \left\{ \langle \rho \rangle^s [v_i] \right\}. \tag{12}$$

The derivation is shown in more detail in the Appendix A.

Independent variables For numerical stability reasons the independent perturbation variables finally used for a reformulation of volume averaged APE are selected based on the prerequisite to be (almost) continuous across an interface between fluid and the porous medium. This way gradients that occur inevitably due to the sudden jump of porosity across the boundary can be lumped together in extra terms linear in the used independent variables which resemble a numerically resolved localized function with a distinct peak across the interface. If applied in conjunction with explicit time integration, these extra terms could trigger numerical instabilities. To circumvent this problem, their contribution can be treated implicitly in a mixed implicit-explicit time integration method (IMEX methods, refer to Ascher et al. [1], Boscarino and Russo [3]), whereas all spatial gradient terms occurring in the governing equations can be treated further on by means of explicit time integration. Since the extra terms are localized, i.e. proportional to the fluctuating variables and do not involve information from neighbor nodes of the computational mesh, implicit treatment in the framework of SDIRK methods (see Ascher et al. [1]) demands only for inversion of an $n \times n$ matrix (depending on the dimension n of the problem) composed out of steady mean-flow variables, which is computed and stored at the begin of an unsteady simulation cycle. Therefore, highly efficient treatment of these implicit gradient terms becomes feasible.

To discuss further the appropriate choice of independent variables, we consider a test set-up of an incompressible channel flow in which a zone of porosity is applied across the channel, refer to Fig. 3. For this case, the intrinsic density in the porous medium, where $0 < \bar{\phi} < 1$ holds, is a constant quantity, since

$$\langle \rho \rangle^i = \frac{\int GH\rho \mathrm{d}^3x}{\int GH \mathrm{d}^3x} = \frac{\rho \int GH \mathrm{d}^3x}{\int GH \mathrm{d}^3x} = \rho. \tag{13}$$

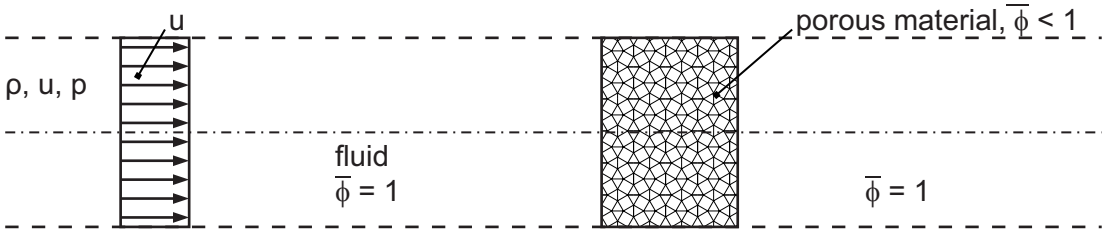

Figure 3: Sketch of channel flow with porous blocking.

Mass conservation across the bulk and in the porosity implies $\rho u = \langle\rho\rangle^s [u] = \text{const}$. Using Eq. (13) and with the help of Eq. (6) this yields

$$u = \bar{\phi}\,[u]\,. \tag{14}$$

Hence, to accomplish almost continuous variables across the fluid-porous interface, we introduce a new velocity variable defined by

$$\hat{v_i} := \bar{\phi}\,[v_i]\,. \tag{15}$$

Furthermore, we chose the intrinsic volume-averaged fluctuating density $\langle\rho\rangle^i$ and the intrinsic volume-averaged fluctuating pressure $\langle p\rangle^i$ to close the set of independent variables.

Volume averaged perturbation equations For the derivation of volume averaged perturbation equations we decompose the volume averaged pressure and density into a mean, i.e. time-averaged, and a fluctuating part. Let ε indicate density or pressure, i.e. $\varepsilon \in \{\rho, p\}$, then the decomposition reads

$$\langle\varepsilon\rangle^{i,s} = \overline{\langle\varepsilon\rangle^{i,s}} + \langle\varepsilon\rangle^{i,s\prime}, \tag{16}$$

where the mean variable is defined by the time-average

$$\overline{a} = \lim_{\Delta t\to\infty} \int_{t_0}^{t_0+\Delta t} a\mathrm{d}t. \tag{17}$$

The Favre volume averaged velocity defined by Eq. (11) is decomposed into a Favre averaged mean-part plus a fluctuation, i.e.

$$[v_i] = \widetilde{[v_i]} + [v_i]''\,, \tag{18}$$

where

$$\widetilde{[v_i]} := \frac{\overline{\langle\rho\rangle^s [v_i]}}{\overline{\langle\rho\rangle^s}}, \tag{19}$$

with the bar indicating a time average, Eq. (17). It is easy to prove that Favre averaging applied to volume averaged quantities still satisfies the usual relations

$$\overline{\langle\rho\rangle^s [v_i]''} = 0 \tag{20}$$

and

$$\overline{\langle\rho\rangle^s [v_i]\,[v_j]} = \langle\rho\rangle^s \widetilde{[v_i]}\widetilde{[v_j]} + \overline{\langle\rho\rangle^s [v_i]''\,[v_j]''}. \tag{21}$$

Superficial volume averaging for density and pressure must be applied to the volume averaged Navier-Stokes equations to enable their reformulation in conservative notation that eventually can be transformed into a formulation based on primitive volume averaged variables, refer to Appendix A. Introduction of the variable decomposition and linearization allows to derive volume averaged perturbation equations in terms of independent variables $\left(\langle\rho\rangle^{s\prime}, [v_i]'', \langle p\rangle^{s\prime}\right)$. For the desired set of independent variables based on intrinsic volume averaged density and pressure as well as velocity defined by Eq. (15), in a final step the variables have to be substituted accordingly. To simplify the syntax, subsequently we will use a notation without additional brackets to indicate intrinsic volume-averaged quantities, e.g. ρ, ρ^0, and ρ' instead of $\langle\rho\rangle^i$, $\overline{\langle\rho\rangle^i}$, and $\langle\rho\rangle^{i'}$, respectively. Furthermore, a simplified notation is introduced for convenience by omitting the overbar on ϕ, i.e. $\overline{\phi} \rightarrow \phi$. Then the substitutions

$$\phi\rho' \rightarrow \langle\rho\rangle^{s\prime}, \quad \phi\rho^0 \rightarrow \overline{\langle\rho\rangle^s}, \quad \phi p' \rightarrow \langle p\rangle^{s\prime}, \quad p^0 \rightarrow \overline{\langle p\rangle^s} \tag{22}$$

have to be applied to eventually reformulate the perturbation equations in the desired set of variables. Proper velocities according to the definition Eq. (15) are obtained by the replacements

$$\frac{\hat{v}_i^0}{\phi} \rightarrow \widetilde{[v_i]}, \quad \frac{\hat{v}_i'}{\phi} \rightarrow [v_i]'' . \tag{23}$$

The extended APE as resulting from consequent application of the volume averaging procedure as outlined before derive as follows: The continuity equation of the APE reads

$$\frac{\partial\rho'}{\partial t} + \phi^{-1}\left[\hat{v}_i^0\frac{\partial\rho'}{\partial x_i} + \hat{v}_i'\frac{\partial\rho^0}{\partial x_i} + \rho^0\frac{\partial\hat{v}_i'}{\partial x_i} + \rho'\frac{\partial\hat{v}_i^0}{\partial x_i}\right] = S_\rho \quad . \tag{24}$$

The APE momentum equation becomes

$$\begin{aligned}
&\frac{\partial\hat{v}_i'}{\partial t} + \phi^{-1}\frac{\partial}{\partial x_i}\left(\hat{v}_k^0\hat{v}_k'\right) + \phi\frac{\partial}{\partial x_i}\left(\frac{p'}{\rho^0}\right) \\
&\quad + \underbrace{\frac{\phi\nu}{\kappa}\delta_{ij}\hat{v}_j'}_{\text{Darcy terms}} + \underbrace{\frac{\phi c_\mathrm{F}}{\sqrt{\kappa}}\sqrt{\hat{v}_k^0\hat{v}_k^0}\left(e_i^0e_j^0 + \delta_{ij}\right)\hat{v}_j'}_{\text{Forchheimer terms}} \\
&\quad + \underbrace{\hat{v}_i^0\hat{v}_j'\frac{\partial}{\partial x_j}\phi^{-1} + \delta_{ij}\hat{v}_j'\hat{v}_k^0\frac{\partial}{\partial x_k}\phi^{-1} - \phi^2\frac{p'}{\rho^0}\frac{\gamma-1}{\gamma}\frac{\partial}{\partial x_i}\phi^{-1}}_{\text{gradient model terms}} = S_{v,i} \quad ,
\end{aligned} \tag{25}$$

where ν denotes the kinetic viscosity, κ identifies the permeability and the Forchheimer coefficient is represented by c_F. It is $\gamma = 1.4$ the isentropic exponent of ambient air. Further, δ_{ij} means the Kronecker delta and e_i^0 indicates the direction of the time averaged mean flow velocity. The inclusion of the Darcy and Forchheimer terms in the governing equations is shown in more detail in Appendix A.

The right-hand source terms of this set of equations are indicated by $S_{\rho,v,p}$. All additional models terms of the momentum equation can be combined to a single matrix $\boldsymbol{\mu}$, such that these terms

are simply added in the form $\mu_{ij}\hat{v}'_j$ to the perturbed momentum equation. The matrix $\boldsymbol{\mu}$ reads

$$\boldsymbol{\mu} = \begin{pmatrix} D+F\left(\frac{\hat{v}_1^0\hat{v}_1^0}{|\boldsymbol{v}^0|^2}+1\right)+\hat{v}_1^0\frac{\partial\phi^{-1}}{\partial x_1}+P & F\frac{\hat{v}_1^0\hat{v}_2^0}{|\boldsymbol{v}^0|^2}+\hat{v}_1^0\frac{\partial\phi^{-1}}{\partial x_2} & F\frac{\hat{v}_1^0\hat{v}_3^0}{|\boldsymbol{v}^0|^2}+\hat{v}_1^0\frac{\partial\phi^{-1}}{\partial x_3} \\ F\frac{\hat{v}_2^0\hat{v}_1^0}{|\boldsymbol{v}^0|^2}+\hat{v}_2^0\frac{\partial\phi^{-1}}{\partial x_1} & D+F\left(\frac{\hat{v}_2^0\hat{v}_2^0}{|\boldsymbol{v}^0|^2}+1\right)+\hat{v}_2^0\frac{\partial\phi^{-1}}{\partial x_2}+P & F\frac{\hat{v}_2^0\hat{v}_3^0}{|\boldsymbol{v}^0|^2}+\hat{v}_2^0\frac{\partial\phi^{-1}}{\partial x_3} \\ F\frac{\hat{v}_3^0\hat{v}_1^0}{|\boldsymbol{v}^0|^2}+\hat{v}_3^0\frac{\partial\phi^{-1}}{\partial x_1} & F\frac{\hat{v}_3^0\hat{v}_2^0}{|\boldsymbol{v}^0|^2}+\hat{v}_3^0\frac{\partial\phi^{-1}}{\partial x_2} & D+F\left(\frac{\hat{v}_3^0\hat{v}_3^0}{|\boldsymbol{v}^0|^2}+1\right)+\hat{v}_3^0\frac{\partial\phi^{-1}}{\partial x_3}+P \end{pmatrix} \tag{26}$$

The following abbreviations have been used therein:

$$\begin{aligned} D &:= \frac{\phi\nu}{\kappa} \\ F &:= \frac{\phi c_{\mathrm{F}}}{\sqrt{\kappa}}\left|\boldsymbol{v}^0\right| \\ \left|\boldsymbol{v}^0\right| &:= \sqrt{(\hat{v}_1^0)^2+(\hat{v}_2^0)^2+(\hat{v}_3^0)^2} \\ P &:= \left(\hat{v}_1^0\frac{\partial\phi^{-1}}{\partial x_1}+\hat{v}_2^0\frac{\partial\phi^{-1}}{\partial x_2}+\hat{v}_3^0\frac{\partial\phi^{-1}}{\partial x_3}+\right) \quad . \end{aligned}$$

The resulting energy equation for the APE in terms of pressure is identical to that one of the LEE:

$$\frac{\partial p'}{\partial t}+\phi^{-1}\left(\hat{v}_i^0\frac{\partial p'}{\partial x_i}+\hat{v}'_i\frac{\partial p^0}{\partial x_i}\right)+\gamma\phi^{-1}\left(p^0\frac{\partial\hat{v}'_i}{\partial x_i}+p'\frac{\partial\hat{v}_i^0}{\partial x_i}\right)+(\gamma-1)\left(p^0\hat{v}'_i+p'\hat{v}_i^0\right)\frac{\partial}{\partial x_i}\phi^{-1}=S_p \quad . \tag{27}$$

It was derived by formal application of volume averaging and reformulating the equation into perturbation form. Further, a thermally and calorically ideal gas was assumed and viscous as well as entropy modes were neglected.

2.3. Fast Random Particle Method (FRPM)

For the simulation of broadband sound generation the APE are excited by stochastically generated right-hand side sources. As the dominating source of vortex sound the fluctuating (linearized) Lamb vector is modeled on the right-hand side of the APE momentum equation, i.e.

$$S_{v,i} = -\epsilon_{ijk}\omega_j^0 v_k^t - \epsilon_{ijk}\omega_j^t v_k^0, \tag{28}$$

where ϵ_{ijk} is the Levi-Civita-symbol. Altogether the system Eqs. (24) to (26) with source (28) constitutes an acoustic analogy based on the wave-operator of irrotational flow, taking into account only the vortex sound source contributions. For the CAA simulations the steady RANS solution is used to prescribe the mean-flow. The mean flow vorticity $\omega_i^0 = \epsilon_{ijk}\partial v_k^0/\partial x_j$ needed to specify the source is computed from the RANS mean-flow velocity. The fluctuating turbulent velocities v_i^t are modeled stochastically with the FRPM method, refer to the next section, from which the fluctuating vorticity is derived as $\omega_i^t = \epsilon_{ijk}\partial v_k^t/\partial x_j$.

The APE suppress the vorticity mode otherwise present in the LEE and as such convective and absolute hydrodynamic instabilities that can plague the LEE are removed, see Ewert and Schröder

[13]. Convecting vorticity can be present in the APE perturbation velocity, but is entirely prescribed by the right-hand side source term. To be precise, vortex sound sources serve on the one hand as a direct sound source, describing the sound generation in free turbulence. On the other hand it acts as a pure vorticity source in the APE. Airframe noise generation is due to the interaction of unsteady convecting turbulence (vorticity) with sharp edges. In previous work with PIANO it was extensively demonstrated, e.g. by injecting test vortices into the linearized Euler equations, that the linear CAA equations are capable of predicting the essential noise sound generation at trailing edges, i.e. the physical conversion process of the vorticity mode into an acoustic mode that take place in the vicinity of geometrical inhomogeneities such as sharp trailing edges, see Lummer et al. [34].

Numerical realization of the FRPM approach In the framework of Random Particle-Mesh methods synthetic turbulence is generated by means of Lagrangian particles distributed over a limited spatial domain where sound sources ought to be realized. The Lagrangian particles are convected by a given steady (or unsteady) background flow. Each particle that crosses an outflow boundary of the source domain will be re-injected at an inflow boundary into the source domain such that the local particle density in the source domain is conserved.

The number of particles necessary to obtain a numerically converged stochastical realization of turbulence was studied in Ewert [10] and Siefert and Ewert [45]. It was found that for locally evaluated particle densities convergence can be achieved for particle numbers exceeding 5 particles per cell (ppc) in 2-D and 10 ppc, respectively. Using a globally specified particle density, minimally 2 ppc are needed for a 2-D problem and 1 ppc in 3-D, refer to R. Ewert [40]. To be precise, for particle densities higher than the previous given values, a solution independent of particle number can be achieved. Unlike stochastic approaches in Fourier space, which aim at realizing a specific (isotropic) turbulence spectra with a given local energy and length scale, FRPM realizes local 2 point correlations of the synthetically generated fluctuating velocity components. In the standard approach, a Gaussian correlation function is realized, thus providing Gaussian turbulence spectra. Via superposition of Gaussian spectra (typically of the order of 10 are used) other turbulence spectra can be realized, e.g. of Liepmann type (see Rautmann et al. [42]) or von-Kármán type (see **?**]), but are not considered in the current publication.

Each particle has associated a set of $i = 1 \ldots n$ random variables; the actual value depends on the dimension of the considered problem. The actual random values attached to each particle will be modified over time by means of a stochastic partial differential equation. The cloud of random particles represents a numerical approximation to spatially delta-correlated white-noise. A fluctuating source component ψ_i is obtained by distributing the ith random deviate r_{ik} of particle k at (variable) position $x\,{}^{c}_{k}(t)$ with a mollifier kernel onto a computational mesh. The numerical approach realizes a weighted sum over all N random particles, Ewert [see 11], defined by

$$\psi_i\left(\boldsymbol{x},t\right) = \sum_{k=1}^{N} \hat{A}^n \mathcal{G}\left(\boldsymbol{x} - \boldsymbol{x}\,{}^{c}_{k}(t)\right) \frac{r_{ik}(t)}{\rho^0(\boldsymbol{x}\,{}^{c}_{k})}. \tag{29}$$

The quantity ρ^0 denotes the mean-flow density ($\boldsymbol{\nabla} \cdot \rho^0 \boldsymbol{u}^0 = 0$). In general, the approach is applicable to compressible fluids of considerable density variation. The amplitude scaling function

$\hat{A}$ can be either a function of $\boldsymbol{x}$ (i.e. depending on the receiver position) or a function of the particle position $\boldsymbol{x}_k^c$. In this work it is chosen to be a function of $\boldsymbol{x}$. The Gaussian filter kernel is defined by

$$\mathcal{G}(\boldsymbol{x} - \boldsymbol{x}_k^c) = \exp\left(-\frac{\pi}{2}\frac{|\boldsymbol{x} - \boldsymbol{x}_k^c|^2}{\Lambda^2}\right), \tag{30}$$

where Λ is the (local) integral length scale of turbulence, corresponding to the amplitude scaling function taken either at position $\boldsymbol{x}$ or $\boldsymbol{x}_k^c$. The properties of the random variables r_{ik} satisfy for frozen turbulence, i.e. in the absence of turbulence decay,

$$\langle r_{ik}(t)\rangle = 0 \tag{31}$$

$$\langle r_{ik}(t) r_{jl}(t)\rangle = \delta_{ij}\delta_{kl}\,\delta m_k \tag{32}$$

$$\dot{r}_{ik} = 0. \tag{33}$$

To summarize the meaning of these equations, r_{ik} represent mutually un-correlated random variables, Eq. (32), with vanishing mean, Eq. (31), and a constant variance proportional to magnitude δm_k, which is an average fluid mass fraction related to each particle, defined by the fluid mass in the source domain divided by the number of particles used in that domain. Furthermore, the particles move with a convection velocity related to the convection velocity field value (typically, the time-averaged mean flow is used to prescribe the convection velocity field) at the actual particle position, i.e.

$$\dot{\boldsymbol{x}}_k^c = \boldsymbol{v}^0\left(\boldsymbol{x}_k^c\right). \tag{34}$$

For frozen turbulence the random variables of each particle remain constant. In case of an exponential decay the properties of the random variable r_{ik} are prescribed by an individual Langevin equation for each random variable and particle, i.e.

$$\dot{r}_{ik} = -\frac{1}{\tau_s} r_{ik} + \sqrt{\frac{2}{\tau_s}} s_{ik}. \tag{35}$$

A (temporal) white-noise source term s_{ik} appears on the right-hand side, with properties

$$\langle s_{ik}(t)\rangle = 0 \tag{36}$$

$$\langle s_{ik}(t) s_{jl}(t+\tau)\rangle = \delta m_k \delta(\tau)\delta_{ij}\delta_{kl}. \tag{37}$$

In other words, s_{ik} represents (temporal) white-noise scaled with a factor of magnitude δm_k. The solution of the Langevin equation (35) with a source having correlation Eq. (37) yields a correlation of variable r_{ik}

$$\langle r_{ik}(t) r_{jl}(t+\tau)\rangle = \delta m_k \delta_{ij}\delta_{kl} \exp\left(-\frac{|\tau|}{\tau_s}\right). \tag{38}$$

The Langevin equation (35) can be solved numerically by the finite-difference equation (see Pope [39, pp. 484]),

$$r_{ik}(t+\Delta t) = \left(1 - \frac{\Delta t}{\tau_s}\right) r_{ik}(t) + \left(\frac{2\delta m_k \Delta t}{\tau_s}\right)^{1/2} \sigma_{ik}(t), \tag{39}$$

where $\sigma_{ik}(t)$ are $m \times N_p$ mutually uncorrelated standardized Gaussian random variables ($\langle \sigma_{ik}(t) \rangle = 0$, $\langle \sigma_{ik}(t)\sigma_{jl}(t) \rangle = \delta_{ij}\delta_{kl}$) which are independent of themselves at different times ($\langle \sigma_{ik}(t)\sigma_{ik}(t') \rangle = 0$, for $t' \neq t$), and which are independent of $r_{ik}(t)$ at past times (e.g., $\langle \sigma_{ik}(t) r_{ik}(t') \rangle = 0$ for $t' \leq t$.

Alternative turbulence decay models using second order Langevin equations have been also proposed, refer to Dieste and Gabard [8], Ewert et al. [16], Neifeld et al. [37], Siefert and Ewert [45]. A correlation function $\mathcal{C}(\boldsymbol{r}, \tau) = \langle \psi_i(\boldsymbol{x}, t)\psi_i(\boldsymbol{x} + \boldsymbol{r}, t + \tau) \rangle / \langle \psi_i(\boldsymbol{x}, t)^2 \rangle$ is related to the filter-kernel function $\mathcal{G}$ via

$$\mathcal{C}(\boldsymbol{r}, \tau) = \int \mathcal{G}(\boldsymbol{r} - \boldsymbol{v}_0^c \tau - \boldsymbol{\xi}) \mathcal{G}(\boldsymbol{\xi}) \mathrm{d}^n \boldsymbol{\xi}. \tag{40}$$

A Gaussian filter kernel

$$\mathcal{G}(x) = \exp\left[-\frac{\pi}{2} \frac{x^2}{\Lambda^2} \right] \tag{41}$$

realizes Gaussian correlations $\mathcal{C}(\boldsymbol{r}, \tau)$ with a width $\sqrt{2}$ times larger than that of the filter kernel. Furthermore Taylor's hypothesis at convection velocity $\boldsymbol{v}_c^0$ is built in:

$$\mathcal{C}(\boldsymbol{r}, \tau) = \exp\left[-\frac{\pi |\boldsymbol{r} - \boldsymbol{v}_c^0 \tau|^2}{4\Lambda^2} \right]. \tag{42}$$

The generation of 3-D isotropic turbulence is achieved by taking fluctuating velocities from the curl of a fluctuating 3-D vector function $\psi_k(x_i, t)$, $k \in \{1, 2, 3\}$,

$$v_i^t = \epsilon_{ijk} \frac{\partial \psi_k}{\partial x_j} \tag{43}$$

For a homogeneous problem the solenoidal velocities v_i^t realize the two-point velocity cross-correlations of homogeneous isotropic turbulence

$$R_{ij}(\boldsymbol{r}, \tau) = \frac{\left\langle v_i^t(\boldsymbol{x}, t) v_j^t(\boldsymbol{x} + \boldsymbol{r}, t + \tau) \right\rangle}{n^{-1} \left\langle v_i^t(\boldsymbol{x}, t)^2 v_i^t(\boldsymbol{x}, t)^2 \right\rangle} = \frac{f(r) - g(r)}{r^2} r_i r_j + g(r) \hat{\delta}_{ij}, \tag{44}$$

where $r = |\boldsymbol{r}|$. In the denominator summation over the equal index product is assumed. Application of the Gaussian kernel yields for the longitudinal correlation function a Gaussian

$$f(r) = \exp\left(-\frac{\pi}{4} \frac{r^2}{\Lambda^2} \right), \tag{45}$$

where the integral length scale is identical to the parameter Λ,

$$L = \int_0^\infty f(r) \mathrm{d}r = \Lambda.$$

The theoretical relation between the longitudinal and lateral correlation functions $f(r)$ and $g(r)$ is given for 3-D homogeneous isotropic turbulence by

$$g(r) = f(r) + \frac{r}{2} \frac{\mathrm{d}f(r)}{\mathrm{d}r}, \tag{46}$$

which is achieved for the stochastic realization, applied to a homogenous problem, in which case the lateral correlation becomes

$$g(r) = \left(1 - \frac{\pi r^2}{4\Lambda^2}\right) \exp\left(-\frac{\pi}{4}\frac{r^2}{\Lambda^2}\right) \tag{47}$$

with lateral length scale $\Lambda/2$. The amplitude $\hat{A}^{(n)}$ in Eq. (29) must be chosen such that the fluctuating velocities achieve a local turbulence kinetic energy $k_T = 1/2\,\langle v_i^t(\boldsymbol{x},t)\langle v_i^t(\boldsymbol{x},t)\rangle$. In 3-D this is accomplished by

$$\hat{A}^{(3)} = \sqrt{\frac{2}{3\pi}\frac{k_T}{\Lambda}}. \tag{48}$$

In a 2-D realization of synthetic turbulence Eq. (29) is applied for $n = 2$ to generate a scalar streamfunction ψ, which defines the two-component velocity field

$$v_i^t = \epsilon_{ij}\frac{\partial \psi}{\partial x_j} \tag{49}$$

with turbulent kinetic energy $k_T = 1/2\,(((v_1^t)^2 + (v_2^t)^2)$. In this case the amplitude function must be scaled according to Ewert [11],

$$\hat{A}^{(2)} = \sqrt{\frac{4k_T}{3\pi}}. \tag{50}$$

3. COMPUTATIONAL SETUP

This chapter presents the grids used for the aerodynamic and the aeroacoustic simulations for both, the solid generic airfoils and that one with a porous trailing edge. Further, the most important parameters necessary for the computions are presented.

3.1. CFD simulations

Generic airfoils RANS CFD simulations as the basis of the CAA simulations were carried out using the unstructured DLR in-house CFD solver TAU, refer to Gerhold et al. [17], Schwamborn et al. [44]. For the NACA0012 airfoil a two-dimensional computational domain is generated, with the outer boundaries extending about 100 chord lengths away from the airfoil. A hybrid grid is chosen, where the viscous sub layer is resolved by a structured region and the parts far away from the airfoil are resolved by a coarser quad-dominated unstructured grid. Along the airfoils surface 225 nodes are distributed along each the upper and lower side. The height of the first cell layer is determined so, that a dimensionless wall distance of $y^+ < 1$ is achieved. The dimensionless tangential distance is $x^+_{\text{nose}} \approx 250$ at the nose, $x^+_{\text{thick}} \approx 1322$ where the airfoil has its greatest thickness and $x^+_{\text{te}} \approx 50$ at the trailing edge. The structured near-airfoil grid extends about 110 layers from the wall with an exponential growth rate. Thus, a good resolution of the viscous sub-layer is realized and so reducing the numerical error for flow variable and turbulence statistic calculations. The hybrid structured/unstructured meshing approach reduces cells in less interesting areas far away from the airfoil and cuts the total number of grid cells to 10^5. The grid,

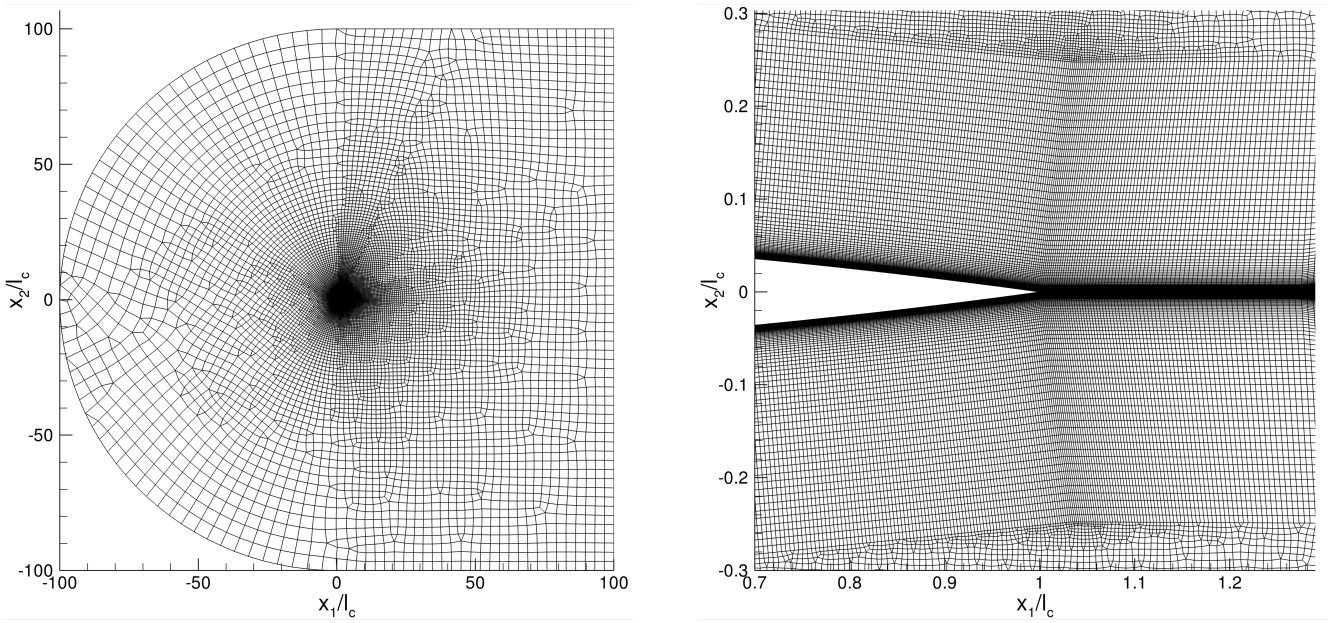

Figure 4: (left) Computational mesh for CFD simulations; (right) detailed view of the structured mesh region near the airfoil.

normalized by the chord length l_c is shown in Fig. 4. The finer resolution in the vicinity of the airfoil is depicted on the right-hand side of Fig. 4.

The airfoils suction and pressure side are defined as viscous walls with a fixed laminar turbulent transition location at $x_{tr} = x_1/l_c = 0.065$ on both sides. The transition is fixed at this position to ensure the same conditions as given by the test case parameters form the experiments, see Herr and Kamruzzaman [27]. A far-field boundary condition with the flow values (U_∞ and α) was applied at the outside boundaries. The two-equation SST-k-ω turbulence model as proposed by Menter [35] was used for the simulation of viscous effects and turbulence statistics.

Porous trailing edges Hybrid RANS based CFD/CAA prediction of aeroacoustic sound generation demands for a suitable RANS solution that also takes into account the effect of porosity on the mean flow and turbulence statistics. A model for simulating porous regions of a computational area was added to DLR in-house CFD solver TAU (see Mößner and Radespiel [36]). With this, a 2-D RANS computation of the flow field around and through a NACA0012 airfoil with a realistic porosity was computed. The porosity was located at the trailing edge and covers the last 11.25% of the airfoil. The numerical setup is depicted in Fig. 5 for the NACA0012 airfoil.

For the 2-D porous trailing edge, a fully structured mesh was built. The computational domain has an extension of $-24.5 \cdot l_c$ in upstream, $29 \cdot l_c$ in downstream and $\pm 26 \cdot l_c$ in vertical direction. The complete mesh consists of $\approx 2.3 \cdot 10^6$ grid points and $\approx 2.15 \cdot 10^6$ elements, respectively. The boundary layer is resolved by about 50 grid points, such that a wall distance of $y^+ < 1$ is achieved. The computational domain for the solid reference case is mainly the same, except for the porous

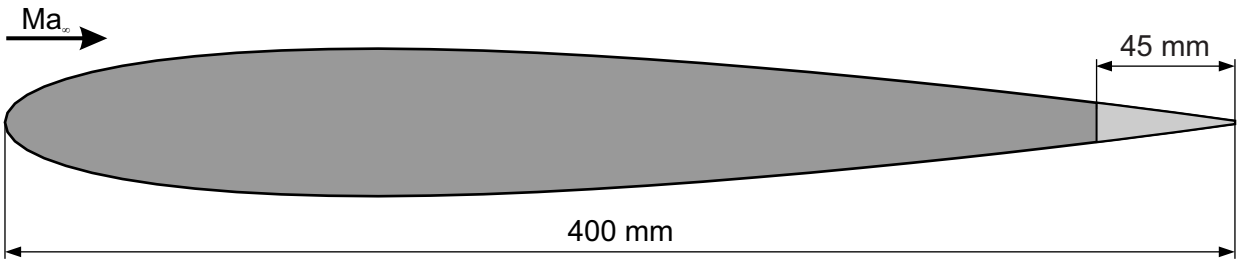

Figure 5: Set up of the porous trailing edge at a NACA0012 geometry at Ma $= 0.118$ and Re $= 1{\cdot}10^6$.

region at the trailing edge. Fig. 6 shows the grid, normalized by the chord length l_c, in an overview and the magnification of the porous resolved region.

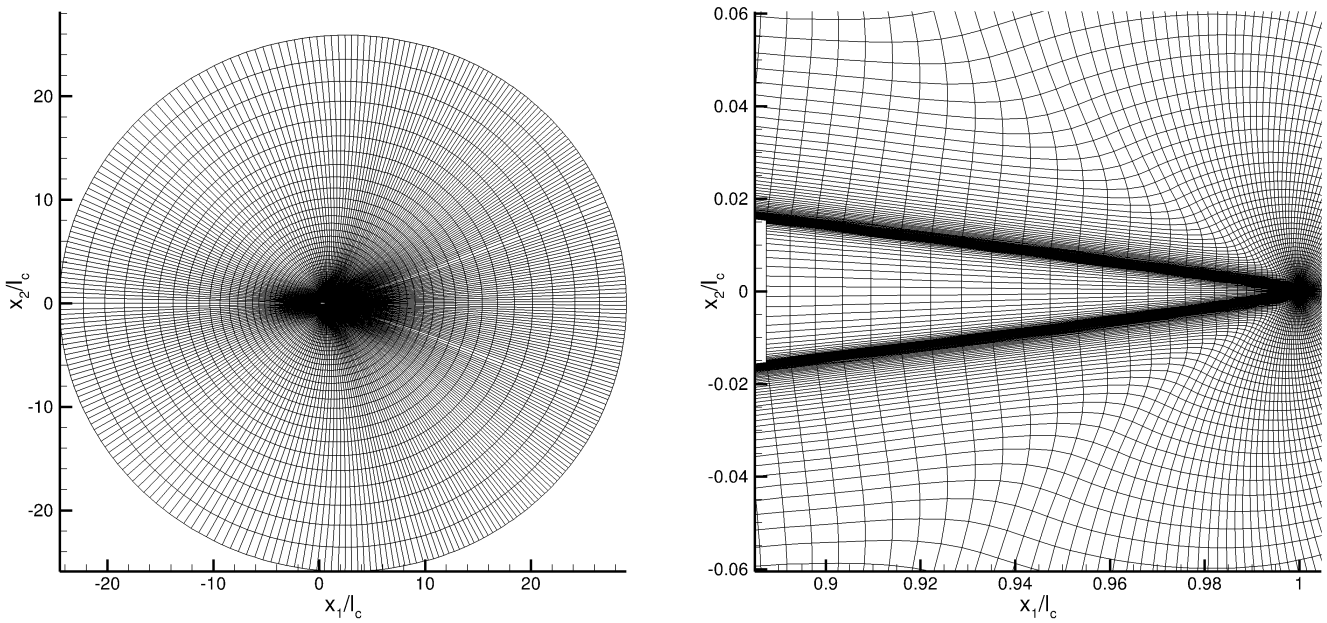

Figure 6: (left) computational mesh for CFD simulations of the porous NACA0012 airfoil; (right) detailed view of the porous region at the trailing edge.

3.2. CAA simulations

Generic airfoils For saving computational time, the 2-D CAA grid has a reduced extension. This is $6 \cdot l_c$ in both streamwise and vertical direction. The structured CAA mesh consists of $\approx 1.1{\cdot}10^6$ grid points, distributed to 64 blocks. The mesh is designed for a field frequency resolution of 10 kHz using 7 points per wavelength resolution. The smallest mesh cells are located in the FRPM area covered by the patch. A timestep of $\Delta t \approx 4.7{\cdot}10^{-7}$ s is used. In total $4{\cdot}10^5$ time steps was simulated resulting in a total real time sampling length of $t \approx 0.19$ s.

Porous trailing edges For the porous trailing-edge test cases, a similar CAA grid was chosen. Only the size of the higher resolved area in the vicinity of the trailing-edge was chosen larger as the porous region at the trailing edge had to be resolved in that case. Thus, an overall cell number

of $\approx 1.5{\cdot}10^6$ grid points was achieved at equal resolution quality. This computational domain is divided into 78 blocks, of which 9 resolve the porous region with about $12.0{\cdot}10^3$ grid points. Fig. 7 shows the grid, normalized by the chord length l_c, in an overview and the magnification of the porous resolved region. The minimal time step allowed is $\Delta t \approx 1.3 \cdot 10^{-7}$ s due to the small cells within the porous region. But, to prevent any numerical instability caused by the porosity model, a smaller time step of $\Delta t \approx 1.2{\cdot}10^{-7}$ s was used. This leads to a roughly 15% higher computational time in total. The computation of $4{\cdot}10^5$ time steps was performed within less than 48 hours on a state-of-the-art cluster system, using 12 CPUs in parallel.

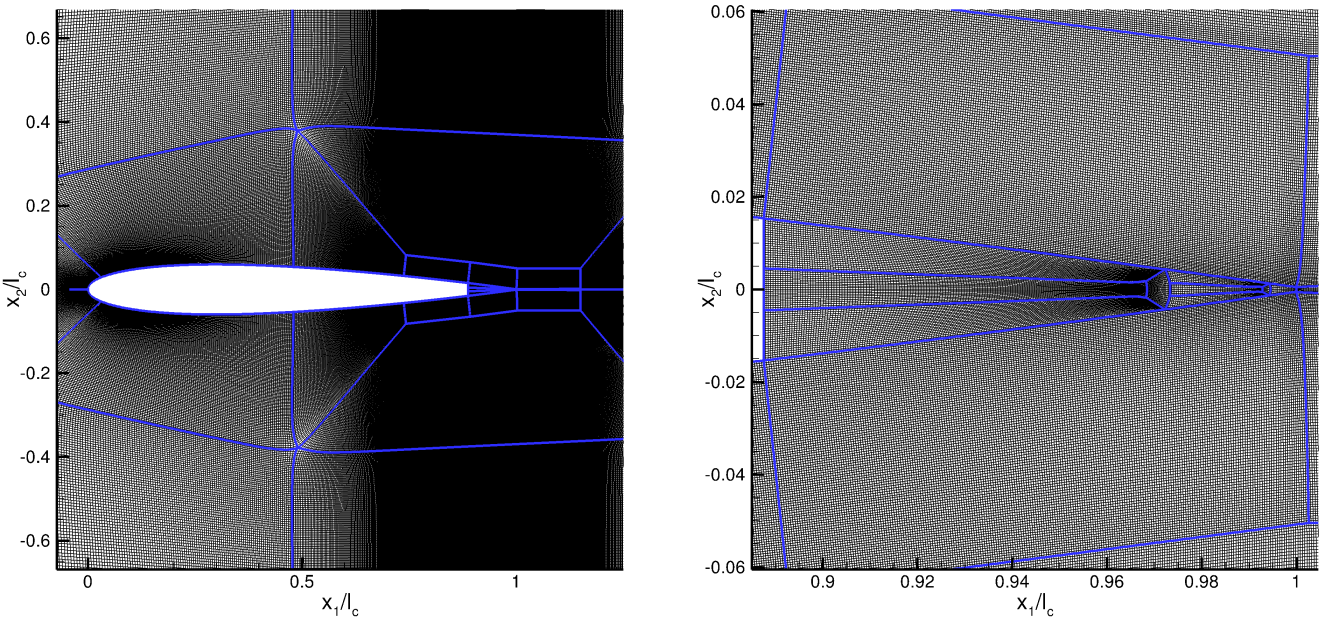

Figure 7: (left) computational mesh for CAA simulations of the porous 2-D airfoil; (right) detailed view of the porous region at the trailing edge.

4. SIMULATION RESULTS

In this chapter, the result of a generic verification of the modified APE is presented. Then, the CFD/CAA approach is discussed in detail. Attention is drawn to the reconstruction of the turbulent statistics with the FRPM model. Finally, the experience from solid airfoils is transfered to the edge noise reduction problem at the trailing edge of a NACA0012 airfoil. The computational results will be compared to measurements, as long as they are available.

4.1. Generic test problems

As a simple verification test case for the implementation of the porous terms, the wave propagation in a quiescent medium is studied for different porous materials. Two different isotropic porosities were chosen: A generic one with artificially chosen porosity parameters and a realistic one with parameters deduced from measurements. The realistic case is based on sintered metals fiber felt. A second test case is wave propagation in an anisotropic porous material without mean-flow. For both

types of verification, the 2-D-computational domain has an extension of $x = -1\,\mathrm{m} \ldots +1\,\mathrm{m}$ and $y = -0.5\,\mathrm{m} \ldots 0.5\,\mathrm{m}$. The fluid phase is ambient air considered as an ideal gas with properties $c_0 = 343\,\mathrm{m/s}$, $p^0 = 1.01325 \cdot 10^5\,\mathrm{Pa}$ and $\rho^0 = 1.205\,\mathrm{kg/m^3}$. The grid is designed to resolve frequencies up to $f = 20\,\mathrm{kHz}$. No additional background damping was used.

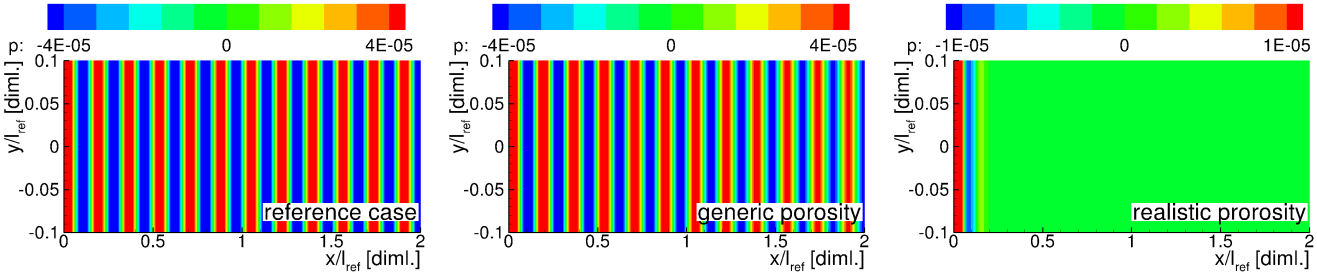

Figure 8: Snapshot of the acoustic response to a harmonic plane wave front at 2 kHz for three different isotropic materials; (left) free medium as a reference, (middle) generic porosity and (right) realistic porosity.

For the first test case with isotropic porosity and a quiescent medium, monofrequent incoming plane waves with different frequencies were specified at the left boundary through a Thompson boundary condition, refer to Thompson [48, 49]. In Fig. 8, a snap shot of the acoustic response is shown for a harmonic signal at 2 kHz. For quantitative evaluation, signals were picked from a horizontal line at $y = 0.1\,\mathrm{m}$.

For a medium at rest, the theoretical damping envelope can be derived from the 1-D wave equation. This is shown in Appendix B, based on the acoustic potential. The damping can be reduced to the ratio of the local root mean square value $\tilde{p}$ of the sound pressure p' to its maximal value at the position x_s of the source, i.e. $\tilde{p}^2 = \overline{(p')^2}$. Considering a homogeneous, isotropic porosity, the damping envelope with respect to x results from Eqs. (82) and (86):

$$\frac{\tilde{p}(x)}{\tilde{p}_{\max}} = \exp\left(-\frac{\omega}{c_0}\sqrt{\frac{1}{2}\sqrt{\frac{(\phi\nu/\kappa)^2}{\omega^2}+1}-\frac{1}{2}}\;x\right) = \exp(\lambda^{(\mathrm{D,sim})}x) \qquad (51)$$

$$\text{with } \tilde{p}_{\max} = \tilde{p}(x_s) \quad .$$

Further, it is L_p the sound pressure level of $\tilde{p}$. Namely it is

$$L_\mathrm{p}^{(\mathrm{D,sim})}(x) = 20\log\left(\frac{\tilde{p}(x)}{\tilde{p}_{\max}}\right) = \frac{20}{\ln(10)}\lambda^{(\mathrm{D,sim})}x \quad . \qquad (52)$$

While the exponent (D) denotes the analytical damping behavior, the exponent (sim) indicates the damping behavior predicted by the simulation. Finally, the degree of agreement between the analytical result and the computiation can be expressed by

$$L_\mathrm{p}^{(\mathrm{sim})} = f(\lambda^{(\mathrm{D})}x) \quad . \qquad (53)$$

In Fig. 9, the results from simulation are juxtaposed to the theoretical decay envelope. The acoustic signal from CAA matches the theoretical damping envelope from Eq. (51) very well.

The plot of the level decay of the rms-values within the computational domain is shown in Fig. 10 in the way introduced by Eq. (53). The computational results fit convincingly well the theoretical

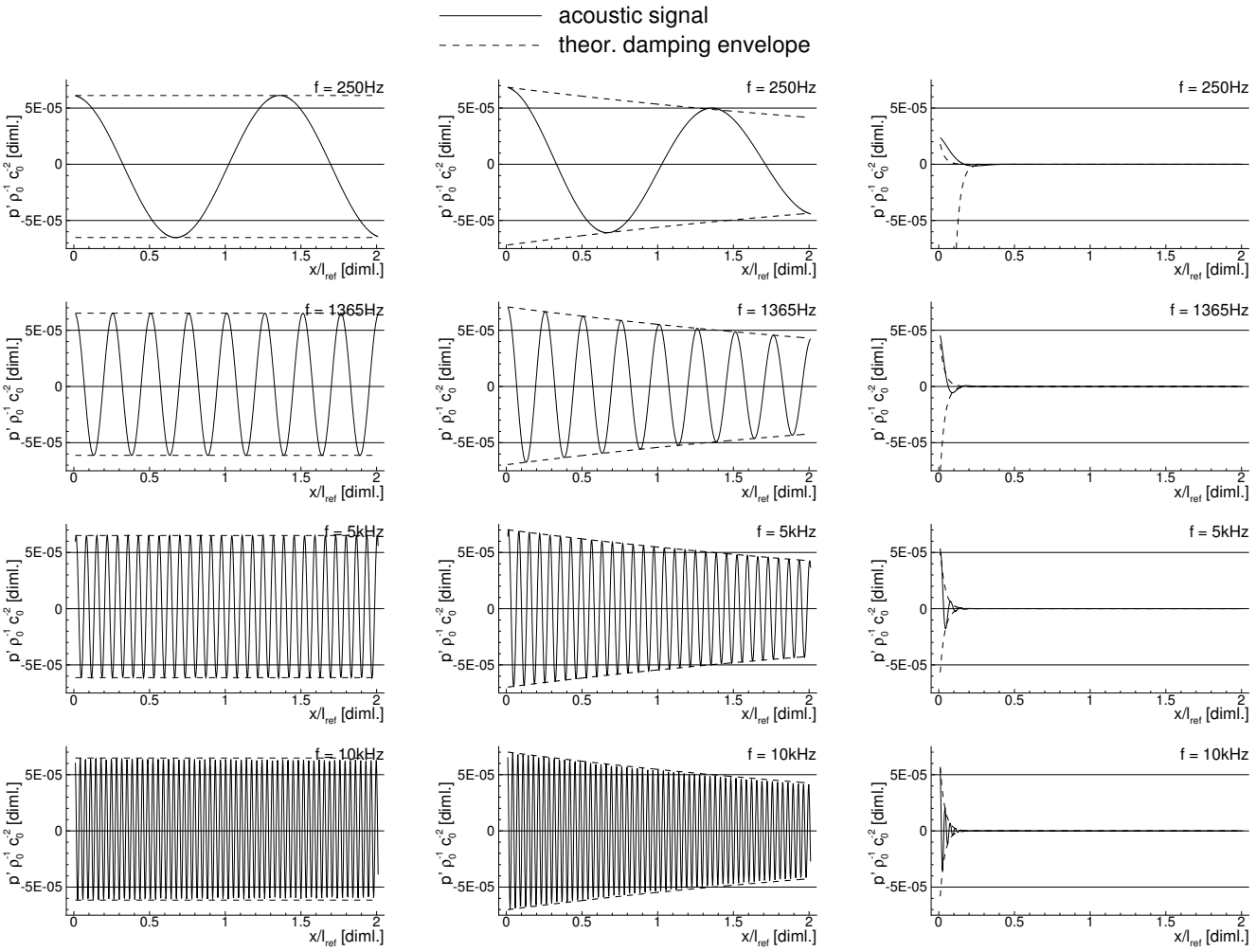

reference case:
$\phi = 1, \frac{\nu}{\kappa} = 0\,\frac{1}{\mathrm{s}}$

generic porosity:
$\phi = 0.8, \frac{\nu}{\kappa} = 2.144{\cdot}10^2\,\frac{1}{\mathrm{s}}$

realistic porosity:
$\phi = 0.86, \frac{\nu}{\kappa} = 26.336{\cdot}10^3\,\frac{1}{\mathrm{s}}$

Figure 9: Comparison of CAA results with Acoustic Pertubation Equations (APE) with theoretical damping envelope of the 1-D wave equation in a medium at rest from Eq. (51) for isotropic porosity.

envelope along the range of 0.25 m. With respect to technical application, this is a good result, as a typical installation depth is less. The prediction accuracy is comparable for a large frequency range.

For the anisotropic porous material, a qualitative evaluation of the computational results is done. The matrix μ_{ij} describing the damping properties was arbitrarily chosen to

$$\mu_{ij} = \begin{bmatrix} 1.0 & 2.0 \\ 2.0 & 5.0 \end{bmatrix} \frac{1}{\mathrm{s}} \tag{54}$$

The resulting eigenvalues $\lambda_{1,2}$ and the related eigenvectors $\boldsymbol{x}_{1,2}$ are:

$$\lambda_1 = 3 - \sqrt{8}\frac{1}{\mathrm{s}} \quad , \quad \boldsymbol{x}_1 = (0.924, -0.383)^T\,\mathrm{m}$$

$$\lambda_2 = 3 + \sqrt{8}\frac{1}{\mathrm{s}} \quad , \quad \boldsymbol{x}_2 = (0.383, 0.924)^T\,\mathrm{m}$$

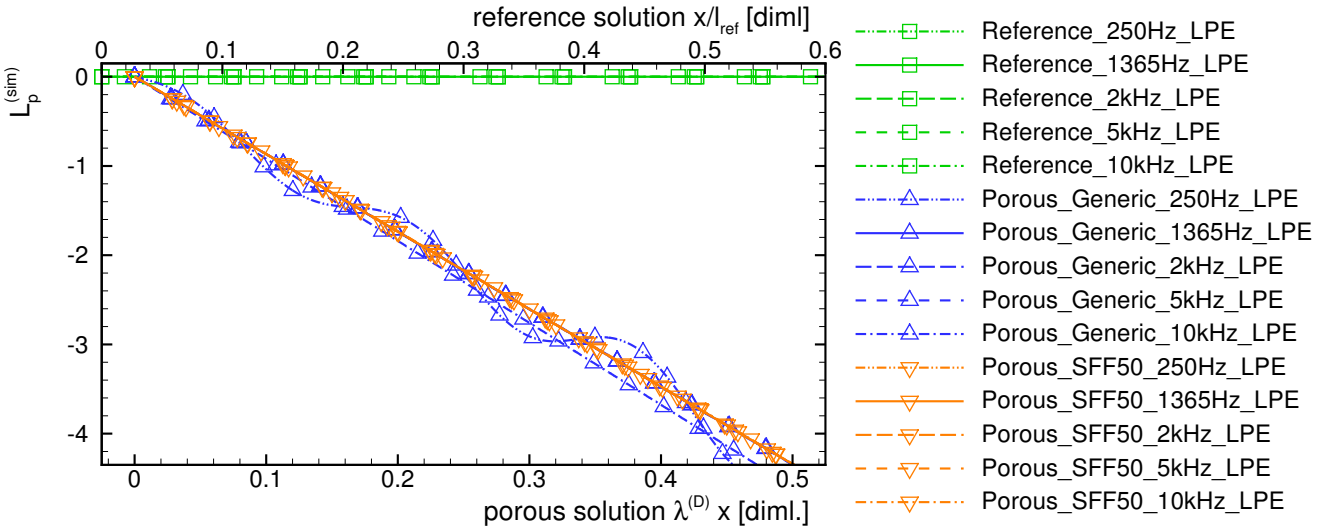

Figure 10: Comparison of CAA results with Acoustic Pertubation Equations (APE) with theoretical damping envelope of the 1-D wave equation in a medium at rest from Eq. (51) for isotropic porosity. For the reference case, the computational prediction is directly given, without comparison with the theoretical damping coefficient, what is $\lambda^{(D)} = 0$ for the free medium.

In Fig. 11, the acoustic response to an harmonic pressure pulse is shown for a material with anisotropic damping properties. The plot illustrates the orientation of the two eigenvectors $\boldsymbol{x}_{1,2}$ and emphasizes that the signal decay along the direction of the first eigenvector $\boldsymbol{x}_1$ is less than the signal decay along $\boldsymbol{x}_2$. This corresponds to the magnitude of the related eigenvalues.

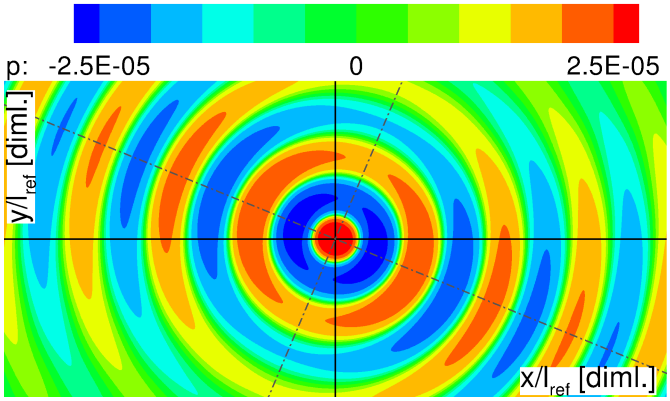

Figure 11: Snap shot of the acoustic response of a anisotropic homogeneous material to an harmonic pressure pulse at a frequency of 1365 Hz; the main axis system is indicated by dashed lines.

The results verify proper implementation of the porous model.

4.2. Generic airfoils

Noise simulations for generic airfoils with the strategy described in the previous part were carried out for the trailing-edge problem statement of the BANC-II workshop, refer to Herr et al. [28].

Herein flow and noise characteristics of 2-D airfoil sections under nominally uniform flow, defined by the flow velocity U_∞ and the angle of attack α, were evaluated from an experimental and a numerical perspective. Measurement data for the validation of numerical codes was made available in the BANC-II problem statement. The computations in this article are mainly focused on test cases #1, #2 and #3, where a NACA0012 airfoil (chord length $l_c = 0.4m$) with different angles of attack under a flow Mach number of Ma = 0.16 and a Reynolds number of $\mathrm{Re}_c = 1.5 \cdot 10^6$ is considered. The angles of attack were ranging from $\alpha = 0\,^\circ$ (case #1) over $\alpha = 4\,^\circ$ (case #2) to $\alpha = 6\,^\circ$ (case #3). Fig. 12 shows boundary layer values simulate by TAU and data from

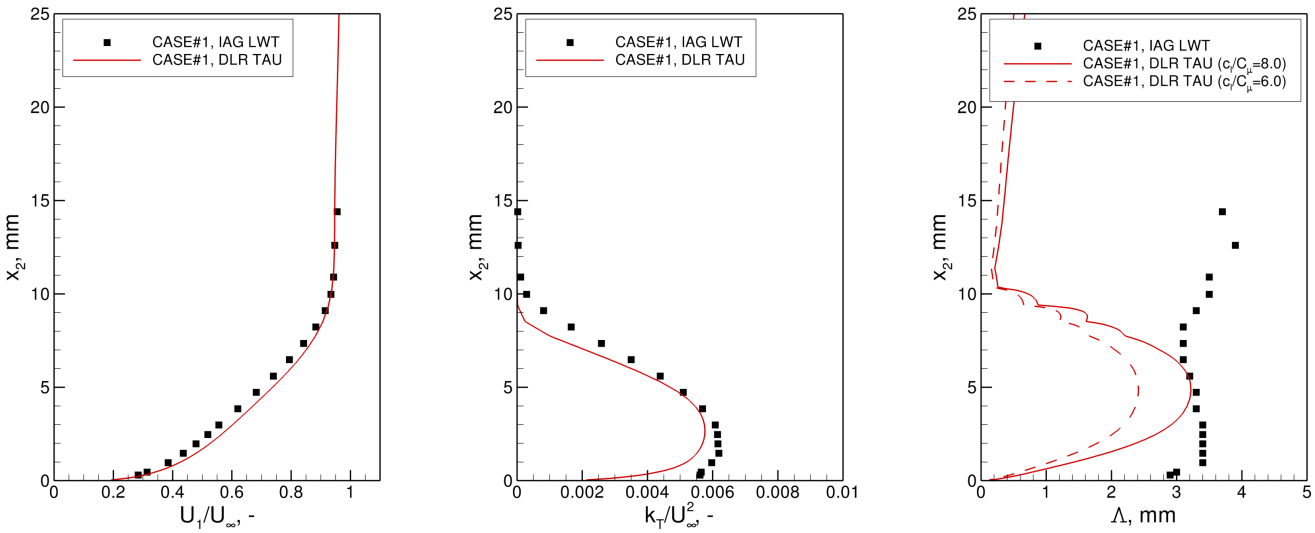

Figure 12: NACA0012 test case #1 ($Ma = 0.16$, $\alpha = 0\,^\circ$) trailing-edge boundary layer profiles; (left) normalized velocity profile in streamwise direction; (middle) normalized turbulent kinetic energy; (right) longitudinal integral length scale for different c_l/C_μ ratios.

the experiments conducted by IAG Stuttgart, Herrig [31]. For the evaluation, the profiles are compared along a vertical line (perpendicular to the airfoil chord) positioned 0.38% main chord behind the airfoils trailing-edge. The NACA0012 zero degree angle of attack test case is chosen for the presentation of the CFD results. The results are in good agreement with the experimental data. The values for the normalized velocity profile in streamwise direction x_1 (Fig. 12 (left)) are in line with the RANS computations. The velocity profile of the TAU simulation shows slightly higher values. However, the general shape and boundary layer thickness (location where $0.99\,U_\infty$ is reached) match quite closely, implying that the used k-ω-SST turbulence model is suitable for this case. Moreover, the non-dimensionalized turbulent kinetic energy profile k_T/U_∞^2 (Fig. 12 (middle)) matches the experimental data. For the used two-equation model with its isotropic turbulence ($\langle u_1' u_1' \rangle = \langle u_2' u_2' \rangle = \langle u_3' u_3' \rangle = \langle u' u' \rangle$) the longitudinal turbulent length scale Λ (see Fig. 12 (right)) can be calculated from the turbulent kinetic energy k_T and the specific dissipation ω :

$$\Lambda = \frac{c_l}{C_\mu} \frac{\sqrt{k_t}}{\omega}. \tag{55}$$

The quantities c_l and C_μ are constants from the turbulence model. The fraction[1] c_l/C_μ is now referred to as c_Λ. It can be observed that, for a $c_\Lambda = 6.0$ the measured length scales (black squares)

[1] for $C_\mu = 0.09$ this implies a value of $c_l = 0.54$

are higher than the computed ones (dashed line). If the ratio is adapted to $c_\Lambda = 8.0$ (solid line), the fitted computational results match the measured values concerning the absolute level. Despite the absolute values of the length scale Λ, the simulated flow field and its turbulence statistics are in good agreement with the experimental values. Concerning the details of the comparison between the measuremts and the prediction of the length scale, a deviation is obvious. Nonetheless, in the region of maximum turbulent kinetic energy, the accordance of the numerical result with the measurement is sufficiently good. This is the region of the most relevance for the reconstruction of the final sound spectra. Thus, a validated and reliable input data set is provided for the following CAA simulations. In the case of non-zero angles of attack, the CFD is underpredicting the profiles of the turbulence statistics. For details refer to Herr et al. [30].

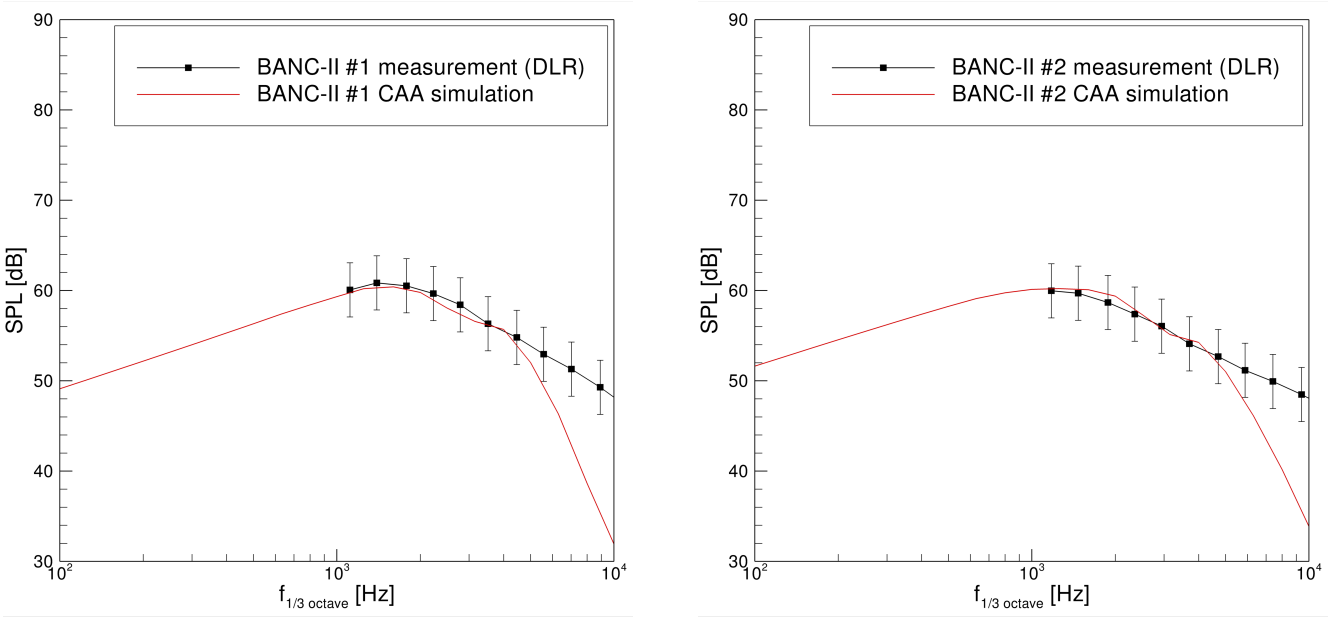

Figure 13: One-third-octave band spectra from CAA simulation compared to available measurement data from BANC-II; (left) test case #1 ($\alpha = 0\,°$); (right) test case #2 ($\alpha = 4\,°$).

Simulated and measured broadband one-third-octave band spectra for the three test cases are shown in Figs. 13 and 14. For the evaluation a microphone position perpendicular to the chord in a distance of $2.5\,l_c$ below the trailing-edge was chosen. Sampling data was recorded every $2.5{\cdot}10^{-5}$ s. For the spectral evaluation a fast Fourier transform with a Hanning window was used. An average of 20 samples was taken to achieve a smoother shape of the curve. The 3 dB uncertainty given by the measurements is indicated by the error bars. For the simulated sound pressure level spectra shown in this section, the 2-D to 3-D correction as proposed by Ewert et al. [14] has been used. Thus, the sound radiation is corrected to account for the 3-D case, as measured in the BANC-II test cases. Untapered, unswept airfoil sections with a wetted span of 1 m were considered. A common off-set calibration of -2.5 dB was used on all simulated CAA spectra. With the chosen best practice setup this additional calibration on top of the 2-D to 3-D correction is needed to match the experimental results in terms of absolute levels.

It can be seen that the CAA spectrum (red line) matches the peak frequency of the experimental data and is in the uncertainty range until approximately 5 kHz for all test cases. Until that point the decay behavior towards high frequencies matches the experimental observations. Beyond this

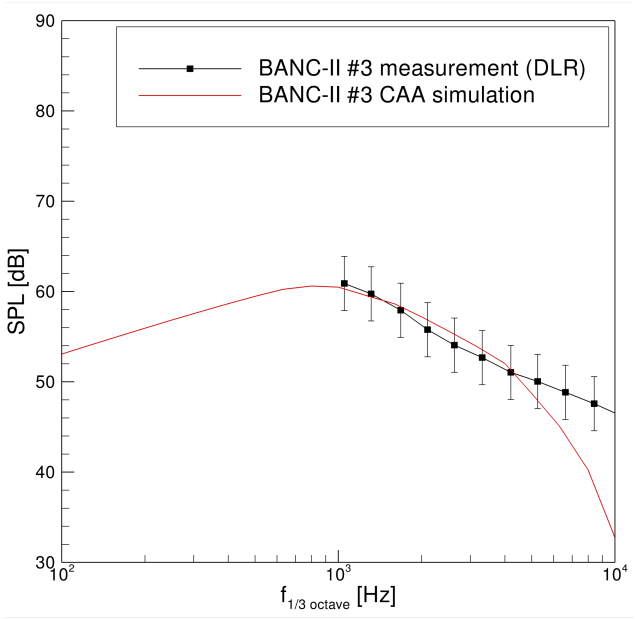

Figure 14: One-third-octave band spectrum from CAA simulation compared to available measurement data from BANC-II; test case #3 ($\alpha = 6\,^{\circ}$).

value the simulated SPL values are lower than in the experiment. A procedure to successfully remedy this problem is currently under investigation, see Rautmann et al. [42]. However, for the low and medium frequency range the procedure is able to correctly predict the broadband noise emitted by the specific airfoil under different operational parameters. For the high frequency range a relative comparison is possible.

For the increasing angle of attack the peak frequency of the spectrum is shifted further towards lower values. Lying at approximately 1.5 kHz for the zero degree angle of attack test case (#1) the peak frequency moves to 0.8 kHz for test case #3 with $\alpha = 6\,^{\circ}$. The general trend of the angle of attack increase is reproduced. The peak frequency shifts towards lower values as for the higher frequencies the SPL values are going up. This is due to the fact that the spectrum is a combination of two single spectra. One low-frequent part coming from the suction side with its relatively wide boundary layer and a second high-frequent part coming from the pressure side with the thin boundary layer. With higher angles of attack, these two spectra become more separated. Hence, the anticipated physical behavior is reproduced by the combined CFD-CAA approach. The computational time for the full sound field around the airfoil was about 15 hours on a 16-CPU machine.

4.2.1. Reconstruction of source statistics

As mentioned in Section 2.1 FRPM realizes turbulent eddies with a local integral length scale Λ. Referring to Eq. (55), Λ can be calculated from the turbulence statistics given by the preliminary conducted CFD simulation. The FRPM turbulence reconstruction has to be limited to a lower length scale l_{min}. The reason for that lies in the spatial resolution of the source patch. The minimum resolved length scale should be greater than four patch cells to avoid numerical errors

due to under resolution of the turbulent eddies. Note, values coming from the CFD solution lower than the chosen l_{min} will be set to the value of l_{min}. It was found that the length scale distribution over the patch has to be smoothed out after cutting it at the minimum value to avoid spurious peaks in the reconstructed TKE spectrum. Results from test case #1 were chosen for illustration. Fig. 15 (left) reveals the Λ field around the trailing edge. The solid line indicates the chosen

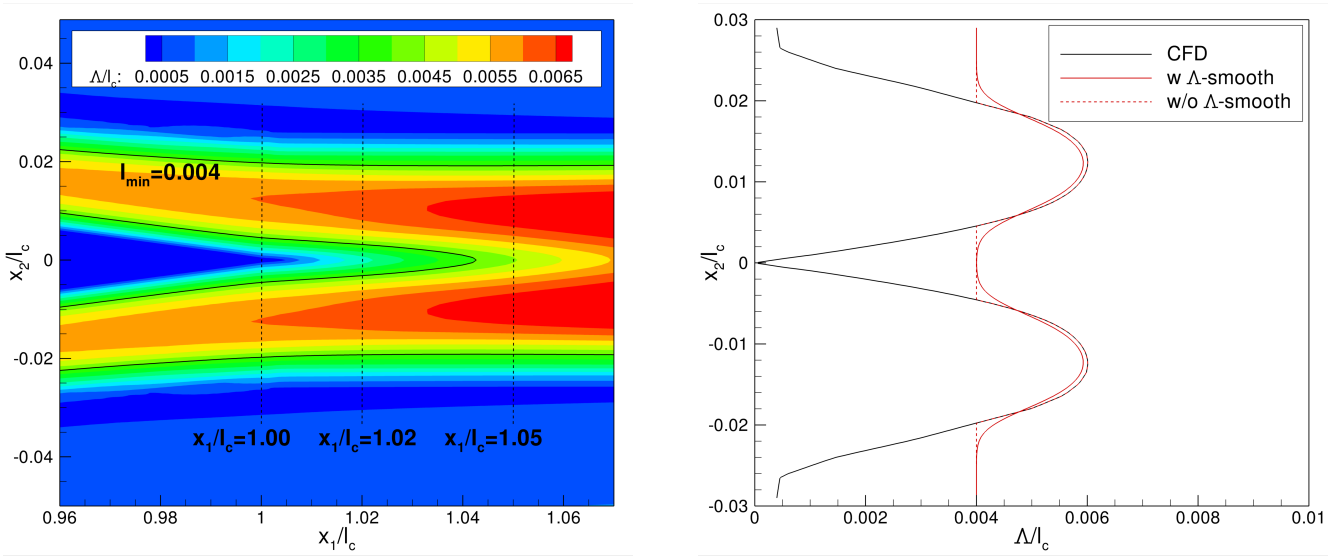

Figure 15: (left) Contour plot of Λ in the vicinity of the TE; (right) different Λ treatments evaluated a $x_1/l_c = 1$.

minimum length scale (in this case $l_{min} = 0.004$). The transition between the variable length scale and the lower threshold l_{min} has to be smoothed in order to avoid a discontinuity in the variable field. The smoothing is shown in Fig. 15 (right). The dashed line shows the unsmoothed Λ-values along a line in x_2 direction directly at the trailing-edge. The effect of the smoothing is shown by the solid line. The influence on the reconstructed TKE distribution is shown in Fig. 16. Compared are similar FRPM simulations once with the length scale smoothing (solid lines) and one without (dashed lines). The evaluation positions refer to the dashed black lines in Fig. 15 (left). It can be seen that the peak in the TKE distribution at the position where the length scale is cut to the lower threshold is reduced by the smoothing of Λ. Also the symmetrical shape for the TKE profile is better reproduced. Only for the last downwind position at $x_1/l_c = 1.05$ the influence is much smaller. This is due to the fact, that there is no cut down of Λ in the inner region of the patch as the values here are all above the threshold. In the outer regions the position were $\Lambda < l_{min}$ is in a region with low turbulent kinetic energy. Thus, no influence is visible. It can be concluded that the new smoothing procedure achieves a better reconstruction of the turbulent field in terms of statistics. This will directly lead to a more precise simulation of the sound sources and the related sound field. Generally speaking, a good reproduction of the turbulent field around the trailing-edge and its statistics was achieved with the FRPM code. Another important thing to consider concerning the length scale is the so called length scale factor c_Λ. Fig. 17 shows the NACA0012 test case calculated with different values of c_Λ. It can be observed, that for the variation of c_Λ the maximum of the spectrum stays at the same frequency of about 1.5 kHz, while there is a severe influence on the slope of the decaying spectra and the SPL values. The higher the value of c_Λ is chosen, the steeper is the slope and the higher are the absolute SPL values.

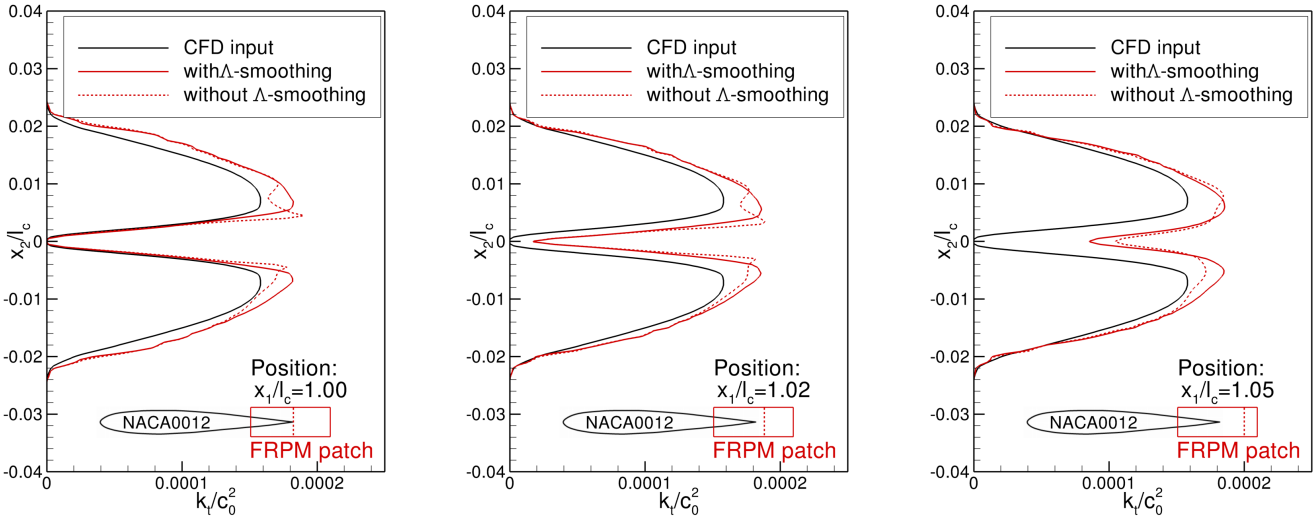

Figure 16: Reconstruction of TKE for NACA0012 ($\alpha = 0\,°$, $Ma = 0.1664$) with different Λ-treatments; (left) normalized TKE at $x_1/l_c = 1.00$; (middle) normalized TKE at $x_1/l_c = 1.02$; (right) normalized TKE at $x_1/l_c = 1.05$.

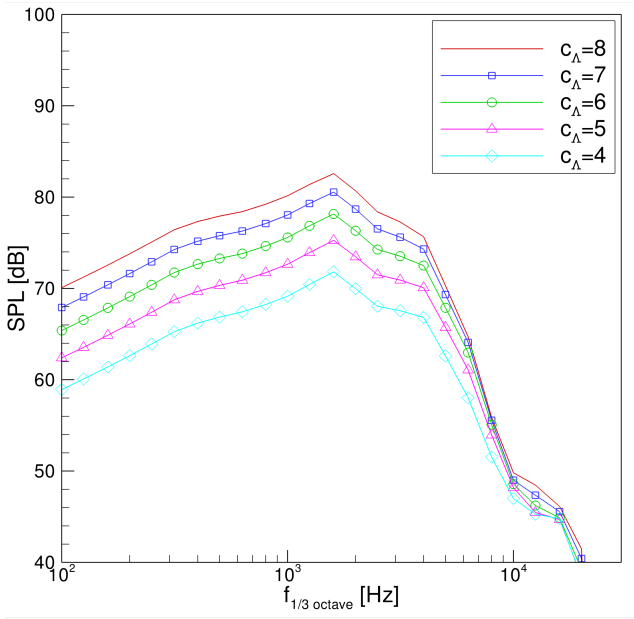

Figure 17: One-third octave sound pressure level spectra for the NACA0012 test case with different values for $c_\Lambda = c_l/C_\mu$, Eq. (55).

For the CAA simulations a c_Λ value of 8 was chosen, as this value matches the measured length scales (see Fig. 12 (right)) and shows good results in turbulence statistic reconstruction. Also, the FRPM grid is able to realize vortices with this length scale.

4.3. Porous trailing edges

The above mentioned technique of porous inlays was then applied to the prediction of the reduction of TBL-TEN due to a porous trailing edge. The realistic properties of the porous material SFF50

were used. In parallel, the reference set-up with solid trailing edge was computed. The predictions were qualitatively and quantitatively evaluated. The snap shot of the sound field comparing the solid reference case and the airfoil with the porous trailing edge in Fig. 18 reveals two details: the porous trailing edge radiates sound at higher frequencies and sound is additionally radiated into direction downstream. For the reference case, the directivity fits the expected behavior of TBL-TEN.

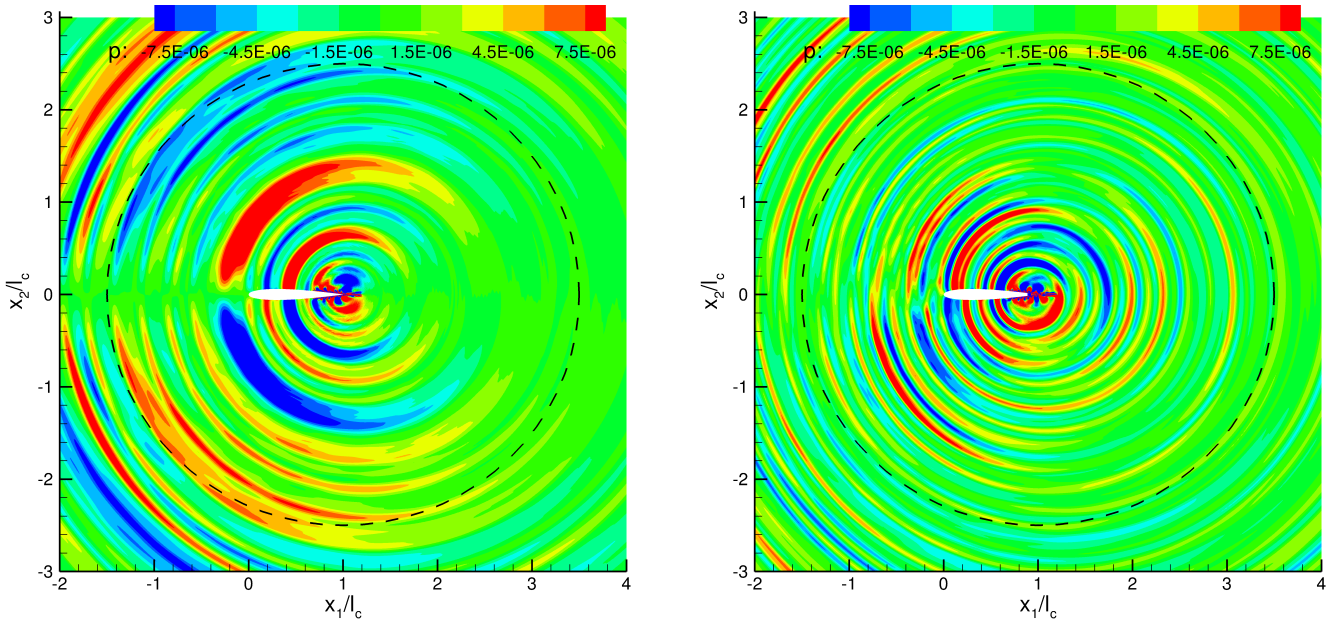

Figure 18: Snap shot of the sound field calculated with CAA by means of FRPM-sources of (left) the solid reference case and (right) a trailing edge with the realistic porosity SFF50. The evaluation microphones are indicated by a dashed circle.

The corresponding directivity is shown in Fig. 19. It gives evidence that radiation of sound in direction downstream occurs. The present data reveal a reduction in direction vertical and upstream of the overall sound pressure level (OASPL) in the range 3 dB. Note, for the evaluation of the shown OASPL only frequencies up to 2.5 kHz were considered.

The spectra presented in Fig. 19 exhibits a sound reduction up to 6 dB in the low frequency range. The sound pressure level for the porous trailing edge exceeds that of the solid trailing edge above 4 kHz. In Herr et al. [29], the experimental results of a cambered F16 airfoil are presented. There, an intersection of the sprectra of the sound pressure levels occurs at frequencies above 10 kHz. The maximum resulting sound reduction during the measurements with the F16 airfoil is about 6 dB to 8 dB. Similar measurements by Herr [26] with a NACA0012 airfoil with narrow lengthwise slits at the trailing edge give a similar result of about 6 dB.

5. SUMMARY AND CONCLUSION

A hybrid CFD-CAA prediction method for the simulation of broadband trailing-edge noise was presented. Details of the underlying theory and the implementation of porous media treatment were given. In a first step, the procedure was used to calculate the acoustic field around a

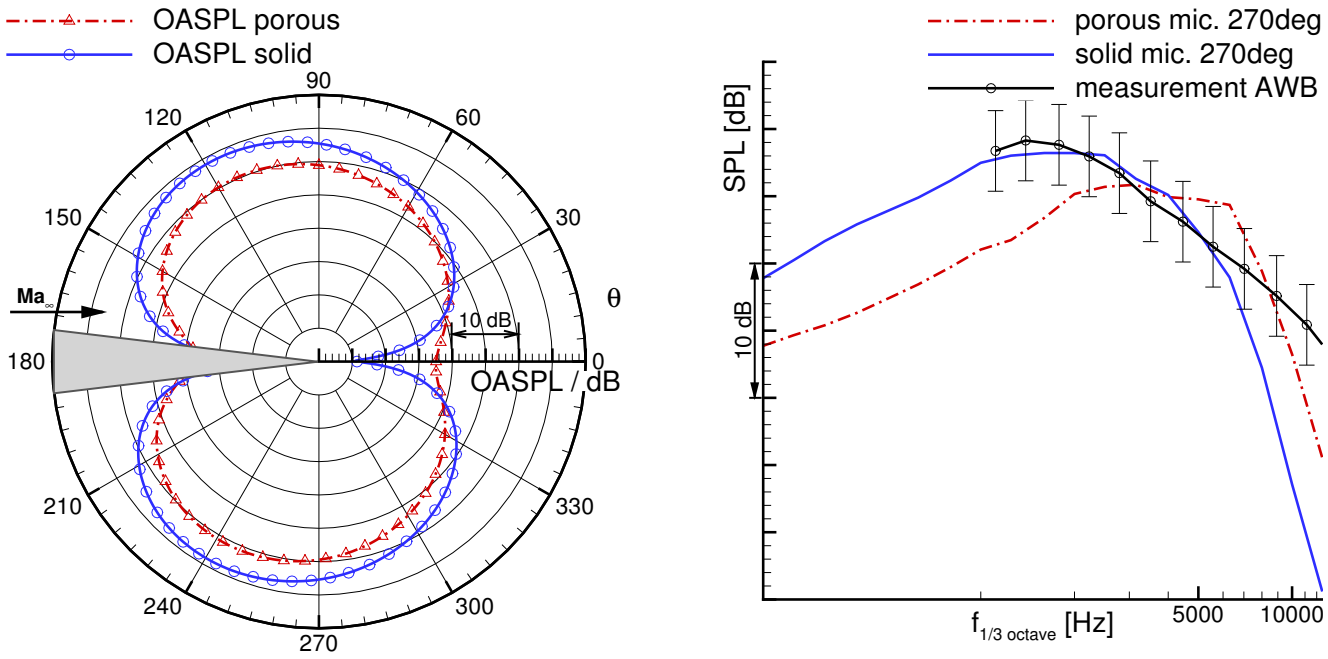

Figure 19: (left) directivity of the overall sound pressure level (OASPL) of the solid reference case compared to the case with porous trailing edge; only frequencies up to 2.5 kHz were considered; (right) resulting one-third-octave band spectra for the two cases at a microphone position 90 deg below the trailing edge compared to a measurement with solid trailing edge, see Herr et al. [28].

NACA0012 airfoil with solid trailing-edge. The mean flow characteristics of the flow field were determined by CFD simulations. It could be shown that acoustic one-third-octave band spectra were in good agreement with experimental data and thus provide a good basis for the following CAA simulations. A closer look was taken on the influence of simulation parameters on the CAA result. A length scale treatment which reduces spurious peaks in the reconstructed turbulence field was presented. Together with this treatment a best practice procedure for trailing-edge noise was achieved. Sound pressure levels calculated by this procedure were in good agreement with measurements from acoustic wind tunnels and thus prove the validity of the method. Beside the capability of solid trailing-edge the simulation the CFD-CAA method was also applied to a porous trailing-edge. For this purpose extended Acoustic Perturbation Equations from volume averaging have been introduced

The method to model porous inlays was tested. To verify the implementation against analytical results, tests of the damping of acoustic waves in homogeneous and anisotropic porous medium were performed first. Further, the porous model was used to predict the sound reduction of an airfoil with porous trailing edge treatment in comparison to a solid airfoil. A decrease of the overall sound pressure level was found for frequencies up to 2.5 kHz. Finally, it was demonstrated, that the present approach is able to calculate physically plausible results within reasonable simulation time.

The only drawback of the actual implementation is the need for a smaller timestep if porous treatment is applied with explicit time integration. To overcome this, an IMEX approach will be implemented as proposed by Ascher et al. [1] and Boscarino and Russo [3]. By this, the 2-D

porous model can be applied without time step limitation.

6. ACKNOWLEDGMENT

Financial support has been provided by the German Research Foundation (Deutsche Forschungsgemeinschaft, DFG) in the framework of the Sonderforschungsbereich 880. Computational resources have been provided by German Aerospace Center (Deutsches Zentrum für Luft- und Raumfahrt e.V., DLR), Institute of Aerodynamics and Flow Technology.

The authors thank Michael Mößner and Kumar Pradeep from Institute of Fluid Mechanics of Technische Universität Braunschweig for providing the CFD of the porous NACA0012 use case.

References

[1] U.M. Ascher, S.J. Ruuth, and R.J. Spiteri. Implicit-Explicit Runge-Kutta methods for time-dependent partial differential equations. *Special Issue on Time Integration*, 25(2–3):151–167, 1997.

[2] K. Bear and M.Y. Corapcioglu, editors. *Fundamentals of Transport Phenomena in Porous Media*. NATO ASI Series. Springer Netherlands, 1984.

[3] S. Boscarino and G. Russo. On the uniform accuracy of IMEX Runge-Kutta schemes and applications to hyperbolic systems with relaxation. In Luigia Puccio, editor, *Communications to SIMAI*, volume 2. Società Italiana di Matematica Applicata e Industriale, 2007.

[4] W.P. Breugem and B.J. Boersma. Direct numerical simulations of turbulent flow over a permeable wall using a direct and a continuum approach. *Physics of Fluids*, 17(2):025103–15, 2005.

[5] T.F. Brooks, D.S. Pope, and M.A. Marcolini. Airfoil self-noise and prediction. Hampton and VA. Langley Research Center.

[6] D.G. Crighton, A.P. Dowling, J.E. Ffowcs Williams, M.A. Heckl, and F.A. Leppington. *Modern Methods in Analytical Acoustics: Lecture Notes*. Springer Berlin, 1996.

[7] J.W. Delfs, M. Bauer, R. Ewert, H. A. Grogger, M. Lummer, and Th.G.W. Lauke. Numerical simulation of aerodynamic noise with DLR's aeroacoustic code PIANO, 2008.

[8] M. Dieste and G. Gabard. Random particle methods applied to broadband fan interaction noise. *Journal of Computational Physics*, 231:8133–8151, 2012.

[9] D.A. Drew. Mathematical modeling of two-phase flow. *Annu. Rev. Fluid Mech.*, 15(1): 261–291, 1983.

[10] R. Ewert. RPM-the fast random particle-mesh method to realize unsteady turbulent sound sources and velocity fields for caa applications. In AIAA/CEAS, editor, *13th AIAA/CEAS Aeroacoustics Conference*, 2007. AIAA Paper 2007-3506.

[11] R. Ewert. Broadband slat noise prediction based on CAA and stochastic sound sources from a fast random particle-mesh (RPM) method. *Computers & Fluids*, 37:369–387, 2008.

[12] R. Ewert and R. Edmunds. CAA slat noise studies applying stochastic sound sources based on solenoidal digital filters. In AIAA/CEAS, editor, *11th AIAA/CEAS Aeroacoustics Conference*, 2005. AIAA Paper 2005-2862.

[13] R. Ewert and W. Schröder. Acoustic perturbation equations based on flow decomposition via source filtering. *Journal of Computational Physics*, 188(2):365–398, 2003.

[14] R. Ewert, C. Appel, J. Dierke, and M. Herr. RANS/CAA based prediction of naca 0012 broadband trailing edge noise and experimental validation. In AIAA/CEAS, editor, *15th AIAA/CEAS Aeroacoustics Conference*, 2009. AIAA Paper 2009-3269.

[15] R. Ewert, J. Dierke, J. Siebert, A. Neifeld, C. Appel, M. Siefert, and O. Kornow. CAA broadband noise prediction for aeroacoustic design. *Computational Aero-Acoustics (CAA) for Aircraft Noise Prediction – PART B*, 330(17):4139–4160, 2011.

[16] R. Ewert, A. Neifeld, and A. Wohlbrandt. A three-parameter Langevin model for hot jet mixing noise prediction. In AIAA/CEAS, editor, *18th AIAA/CEAS Aeroacoustics Conference*, 2012. AIAA 2012-2238.

[17] T. Gerhold, M. Galle, O. Friedrich, and J. Evans. Calculation of complex three-dimensional configurations employing the DLR-tau-code. In *35th Aerospace Sciences Meeting and Exhibit*, 1997.

[18] W.G. Gray. A derivation of the equations for multi-phase transport. *Chemical Engineering Science*, 30(2):229–233, 1975.

[19] W.G. Gray and P.C.Y. Lee. On the theorems for local volume averaging of multiphase systems. *International Journal of Multiphase Flow*, 3(4):333–340, 1977.

[20] GWEC. Global wind report 2012: Annual market update 2012, 2012.

[21] M. Hassanizadeh and W.G. Gray. General conservation equations for multi-phase systems: 1. averaging procedure. *Advances in Water Resources*, 2:131–144, 1979.

[22] W.G. Hassanizadeh, M.and Gray. General conservation equations for multi-phase systems: 2. mass, momenta, energy, and entropy equations. *Advances in Water Resources*, 2:191–203, 1979.

[23] E. Hau. *Windkraftanlagen: Grundlagen, Technik, Einsatz, Wirtschaftlichkeit*. Springer Berlin, 2014.

[24] R.E. Hayden. Reduction of noise from airfoils and propulsive lift systems using variable impedance systems: Palo alto, ca, july 20 - 23, 1976. In AIAA, editor, *3rd AIAA Aeroacoustics Conference*, 1976. AIAA paper 76487-76588.

[25] R.E. Hayden and R.C. Chanaud. Foil structures wirh reduces sound, 1974.

[26] M. Herr. Design criteria for low-noise trailing-edges. In AIAA/CEAS, editor, *13th AIAA/CEAS Aeroacoustics Conference*, 2007. AIAA Paper 2007-3470.

[27] M. Herr and M. Kamruzzaman. Benchmarking of trailing-edge noise computations – outcome of the BANC-II workshop. 2013.

[28] M. Herr, C. Bahr, and M. Kamruzzaman. Workshop category 1: Trailing-edge noise. problem statement for the AIAA/CEAS. In *2nd Workshop on Benchmark Problems for Airframe Noise Computations (BANC-II)*, 2012.

[29] M. Herr, K.-S. Rossignol, J.W. Delfs, M. Mößner, and N. Lippitz. Specification of porous materials for low-noise trailing-edge applications. In AIAA/CEAS, editor, *20th AIAA/CEAS Aeroacoustics Conference*, pages AIAA Paper 2014–XXXX, 2014.

[30] M. Herr, R. Ewert, C. Rautmann, M. Kamruzzaman, D. Bekiropoulos, R. Arina, A. Iob, P. Batten, S. Chakravarthy, and F. Bertagnolio. Broadband trailing-edge noise predictions — overview of BANC-III results. In AIAA/CEAS, editor, *submitted to 21th AIAA/CEAS Aeroacoustics Conference*, 2015.

[31] A. Herrig. *Validation and application of a hot-wire based method for trailing-edge noise measurements on airfoils: Doctoral thesis*. Stuttgart, 2011.

[32] M.S. Howe. On the added mass of a perforated shell, with application to the generation of aerodynamic sound by a perforated trailing edge. *Proceedings of the Royal Society of London. A. Mathematical and Physical Sciences*, 365(1721):209–233, 1979.

[33] M.S. Howe. *Theory of vortex sound*. Cambridge University Press, 2003.

[34] M. Lummer, J.W. Delfs, and T. Lauke. Simulation of the influence of trailing edge shape on airfoil sound generation. In AIAA/CEAS, editor, *9th AIAA/CEAS Aeroacoustics Conference*, 2003. AIAA Paper 2003–3109.

[35] F. R. Menter. Two-equation eddy-viscosity turbulence models for engineering applications. *AIAA Journal*, 32(8):1598–1605, 1994.

[36] M. Mößner and R. Radespiel. Numerical simulations of turbulent flow over porous media. In AIAA, editor, *21st AIAA Computational Fluid Dynamics Conference*, 2013. AIAA Paper 2013-2963.

[37] A. Neifeld, R. Ewert, M. Steger, and M. Rose. Prediction of Hot Jet Mixing Noise Using Extended Stochastic Source Correlations. In AIAA/CEAS, editor, *19th AIAA/CEAS Aeroacoustics Conference*, 2013. AIAA 2013-2040.

[38] J. Ni and C. Beckermann. A volume-averaged two-phase model for transport phenomena during solidification. *Metallurgical Transactions B*, 22(3):349–361, 1991.

[39] S. B. Pope. *Turbulent Flows*. Cambridge University Press, 2000.

[40] J. Held T. Leicht M. Bauer G. Ashcroft C. Weckmüller S. Guerin A. Schady D. Heimann M. Siefert O. Heintze O. Unruh B. Mühlbauer B. Noll R. Ewert, R. Hartmann. Schlußbericht AVANTGARDE. Technical report, German Aerospace Center(DLR), 2010.

[41] R. Radespiel and W. Heinze. SFB 880 – Fundamentals of High-Lift for Future Commercial Aircraft. In *Deutscher Luft- und Raumfahrtkongress 2013*. DGLR, Deutsche Gesellschaft für Luft-u Raumfahrt, 2013.

[42] C. Rautmann, J. Dierke, R. Ewert, N. Hu, and J. Delfs. Generic airfoil trailing-edge noise prediction using stochastic sound sources from synthetic turbulence. In AIAA/CEAS, editor, *20th AIAA/CEAS Aeroacoustics Conference*, pages AIAA Paper 2014–XXXX, 2014.

[43] J.G. Schepers, A. Curvers, S. Oerlemans, K. Braun, T. Lutz, A. Herrig, W. Wuerz, A. Mantesanz, L. Garcillán, M. Fisher, K. Koegler, and T. Maeder. Sirocco: Silent rotors by acoustic optimisation, 2007.

[44] D. Schwamborn, T. Gerhold, and R. Heinrich. The DLR tau-code: Recent applications in research and industry. In *Proc. of Europ. Conf. on Computational Fluid Dynamics ECCOMAS CFD*, 2006.

[45] M. Siefert and R. Ewert. Sweeping sound generation in jets realized with a random particle-mesh method. In AIAA/CEAS, editor, *15th AIAA/CEAS Aeroacoustics Conference*, 2009. AIAA Paper 2009-3369.

[46] J.C. Slattery. Single-phase flow through porous media. *AIChE Journal*, 15(6):866–872, 1969.

[47] C.K.W. Tam and J.C. Webb. Dispersion-relation-preserving finite difference schemes for computational acoustics. *Journal of Computational Physics*, 107(2):262–281, 1993.

[48] K.W. Thompson. Time dependent boundary conditions for hyperbolic systems. *Journal of Computational Physics*, 68(1):1–24, 1987.

[49] K.W. Thompson. Time-dependent boundary conditions for hyperbolic systems, ii. *Journal of Computational Physics*, 89(2):439–461, 1990.

[50] S. Wagner, R. Bareiss, and G. Guidati. *Wind Turbine Noise*. Springer, Berlin and and New York, 1996.

[51] S. Whitaker. The transport equations for multi-phase systems. *Chemical Engineering Science*, 28(1):139–147, 1973.

A. PROPERTIES OF VOLUME AVERAGING

One property of volume averaging is that it is interchangeable with summation, i.e.

$$\langle a+b\rangle^{i,s} = \langle a\rangle^{i,s} + \langle b\rangle^{i,s}\,. \tag{56}$$

It follows directly from the definition Eq. (1) (just shown for the superficial component)

$$\langle a+b\rangle^{s} = \frac{\int G\,(a+b)\,d^3x'}{V_\Delta} = \frac{\int G a d^3x'}{V_\Delta} + \frac{\int G b d^3x'}{V_\Delta} = \langle a\rangle^{s} + \langle b\rangle^{s}\,. \tag{57}$$

Commutation of volume averaging and time differentiation follows immediately from the definitions Eqs. (1) and (3), i.e.

$$\left\langle \frac{\partial \rho}{\partial t} \right\rangle^{s} = \frac{1}{V_\Delta}\int \frac{\partial\, GH\rho}{\partial t} d^3x' = \frac{\partial}{\partial t}\frac{1}{V_\Delta}\int GH\rho\, d^3x' = \frac{\partial}{\partial t}\langle\rho\rangle^{s}\,. \tag{58}$$

Commutativity of volume and averaging with respect to spatial differentiation can be also derived from definition Eq. (1),

$$\begin{aligned}\left\langle \frac{\partial \rho v_i}{\partial x_i} \right\rangle^s &= \frac{\int G\left(\boldsymbol{x}-\boldsymbol{x}',\Delta\right) \frac{\partial}{\partial x_i'} \left\{\rho v_i(\boldsymbol{x}',t)\right\} H(f(\boldsymbol{x}'))d^3x'}{\int G\left(\boldsymbol{x}-\boldsymbol{x}',\Delta\right) d^3x'} \\ &= \frac{\int G \frac{\partial}{\partial x_i'} \left\{\rho v_i(\boldsymbol{x}',t) H(f(\boldsymbol{x}'))\right\} d^3x'}{\int G d^3x'} - \underbrace{\frac{\int G \rho v_i \frac{\partial f}{\partial x_i'} \delta(f(\boldsymbol{x}'))d^3x'}{\int G d^3x'}}_{(i)}.\end{aligned} \tag{59}$$

The Dirac delta function in the second of the finally resulting terms results from the spatial derivation of the Heaviside function, i.e. $\partial/\partial x_i(H(f)) = \delta(f)\partial f/\partial x_i$. The volume integration over the delta function reduces the volume integral to a surface integral over all boundaries between solid and fluid phase, where $f = 0$. Since the gradient of f is normal to the surface, $\partial f/\partial x_i = n_i$—refer to Fig. 2—the wall normal velocity, i.e. the scalar product of velocity with the wall normal, vanishes ($v_n = v_i n_i = 0$) due to the no-slip condition of the velocity and thus the entire second term (i) vanishes.

The remaining terms can be manipulated further, i.e.

$$\begin{aligned}\int G \frac{\partial \rho v_i H(f)}{\partial x_i'} d^3x' &= \underbrace{\int \frac{\partial}{\partial x_i'} \left\{G \rho v_i H(f)\right\} d^3x'}_{Ia} - \underbrace{\int \frac{\partial G}{\partial x_i'} \rho v_i H(f) d^3x'}_{Ib} \\ &= \underbrace{\int \frac{\partial G}{\partial x_i} \rho v_i H(f) d^3x'}_{II} = \underbrace{\frac{\partial}{\partial x_i}\left[\int G \rho v_i H(f) d^3x'\right]}_{III}\end{aligned} \tag{60}$$

In a first step the differentiation has been shifted to the filter kernel. By means of Gauss theorem the first integral (Ia) will vanish, since the filter function decays for large magnitudes of its argument towards zero. Due to the dependence of the filter function on argument $\boldsymbol{x} - \boldsymbol{x}'$, a derivative with respect to x_i' on G can be changed into a derivative with respect to x_i. This has been applied to proceed from Ib to II. In step III, the derivative is shifted out of the integral. Taking into account the last integral, and utilizing that a Gaussian filter function (which is even) satisfies[2]

$$\frac{\partial}{\partial x_i} \int G d^3x' = \int \frac{\partial G}{\partial x_i} d^3x' = -\int \frac{\partial G}{\partial x_i'} d^3x' = 0, \tag{61}$$

it follows

$$\left\langle \frac{\partial \rho v_i}{\partial x_i} \right\rangle^s = \frac{\partial}{\partial x_i} \left\{\langle\rho\rangle^s \left[v_i\right]\right\} = \frac{\partial}{\partial x_i} \langle \rho v_i \rangle^s = \frac{\partial}{\partial x_i} \left\{ \frac{\int G \rho v_i H(f) d^3x'}{\int G d^3x'} \right\}. \tag{62}$$

This result proves commutativity of superficial volume averaging and spatial differentiation for the term ρv_i, Eq. (12). Note, strict satisfaction of commutativity is a result of the no-slip condition that causes the vanishing of term (i) in Eq. (59). For other terms this is not in general the case.

[2]The property Eq. (61) would not hold in general for intrinsic volume averaged quantities, since for the denominator $\partial/\partial x_i \int G H(f) \mathrm{d}^3x'$ it cannot be guaranteed that it is always identical zero.

For example, the previous steps applied to variable pressure p instead of ρv_i yields for this term (i)

$$f_i^p = \frac{\int G\ pn_i\ \delta(f(\boldsymbol{x}'))d^3x'}{V_\Delta} = \frac{1}{V_\Delta}\int\limits_S G\ pn_i\ dS. \tag{63}$$

This represents the pressure force from the solid onto the fluid. Consequent application of the volume averaging procedure to the continuity and momentum equation yields

$$\left\langle \frac{\partial \rho}{\partial t} + \frac{\partial \rho v_i}{\partial x_i} \right\rangle^s = \frac{\partial \langle\rho\rangle^s}{\partial t} + \frac{\partial}{\partial x_i}\left\{\langle\rho\rangle^s [v_i]\right\} = 0 \tag{64}$$

and

$$\left\langle \frac{\partial \rho v_i}{\partial t} + \frac{\partial \rho v_i v_j}{\partial x_j} + \frac{\partial p}{\partial x_i} - \frac{\partial \tau_{ij}}{\partial x_j} \right\rangle^s = \tag{65}$$

$$\frac{\partial \langle\rho\rangle^s [v_i]}{\partial t} + \frac{\partial \langle\rho\rangle^s [v_i]\,[v_j]}{\partial x_j} + \frac{\partial \langle p\rangle^s}{\partial x_i} - \frac{\partial \langle\tau_{ij}\rangle^s}{\partial x_j} - \mathcal{F}_i = 0$$

with

$$\mathcal{F}_i = f_i - \underbrace{\frac{\partial(\rho v_i v_j - \langle\rho\rangle^s [v_i]\,[v_j])}{\partial x_j}}_{SFS}. \tag{66}$$

Here the interchangeability of volume averaging and summation has been applied. Furthermore, for all gradient terms commutativity of volume averaging and differentiation has been used.

The volume force f_i represents the effect of term (i) from pressure p as shown by Eq. (63) and a similar shear stress contribution from τ_{ij}. Due to the no-slip condition satisfied by velocity, the term $\rho v_i v_j$ will provide no contribution to f_i. Note, volume averaging in general creates the sub-filter stress (SFS) indicated above from the sub-filter velocity fluctuations $v_i'' = v_i - [v_i]$. The sub-filter velocity component must be distinguished from the Favre fluctuations of the volume averaged velocity defined in Eq. (18). To be precise, the complete velocity is given by

$$v_i = \widetilde{[v_i]} + [v_i]'' + v_i''. \tag{67}$$

The volume force term and sub-filter contributions inside the porous medium are modeled by the ansatz proposed by Darcy and Forchheimer. The Darcy terms describes a velocity proportional volume force, whereas the Forchheimer term explicitly addresses a quadratic contribution to the force,

$$-\mathcal{F}_i = \underbrace{\phi\frac{\langle\mu\rangle^s}{\kappa}[v_i]}_{\text{Darcy terms}} + \underbrace{\langle\rho\rangle^s\,\phi^2\frac{c_\mathrm{F}}{\sqrt{\kappa}}\sqrt{[v_k][v_k]}[v_i]}_{\text{Forchheimer terms}} \quad , \tag{68}$$

where ϕ denotes the porosity, μ is the dynamic viscosity, κ identifies the permeability and the Forchheimer coefficient is indicated by c_F.

Despite the additional terms, the resulting momentum equation corresponds formally with the Navier-Stokes equations in conservative form. They can be reformulated in primitive form. For example, the momentum equation is rewritten into an equation for the time derivative of velocity

by removing with the help of the continuity equation the time derivative of density. The independent variables can be split further into resolved Favre averaged and fluctuating components for the velocity, i.e. Eq. (18), and mean and fluctuating components for pressure and density as defined by Eq. (16). Introducing the decomposition into the equations in primitive notation yields non-linear equations in disturbance form. Next, mean flow terms can be neglected by subtracting the mean of a disturbance equation from itself. Finally, non-linear terms might be neglected. This way, the governing equations can be reformulated into perturbation form as shown in Section 2.2. For example, the volume averaged continuity equations is rewritten as

$$\frac{\partial \langle \rho' \rangle^{s'}}{\partial t} + \frac{\partial}{\partial x_i} \left\{ \langle \rho \rangle^{s'} \widetilde{[v_i]} + \overline{\langle \rho \rangle^{s}} \, [v_i]'' \right\} = 0 \tag{69}$$

Utilizing the notation as introduced by Eqs. (22) and (23), the previous equation agrees with Eq. (24). For the derivation of the momentum equation in the from used in the APE (with some left-hand side terms shifted to the right-hand side to define appropriate vortex sound sources), the Darcy and Forchheimer terms have to be linearized as well, finally yielding the equation as outlined in Eq. (25). The APE pressure equation is obtained by substituting ρ' with p'/c_0, where c_0 denotes the speed of sound in the free fluid.

It may be emphasized (without explicit proof) that for a Gaussian filter function

$$G_\Delta \left(\boldsymbol{x} - \boldsymbol{x}', \Delta \right) = \frac{1}{\left(2\pi\right)^{3/2} \Delta^3} \exp \left[- \frac{\left| \boldsymbol{x} - \boldsymbol{x}' \right|^2}{2\Delta^2} \right], \tag{70}$$

the consecutive application of volume averaging to variable a with different length scales for each filter step, i.e.

$$\left\langle \langle a \rangle^s_{\Delta_1} \right\rangle^s_{\Delta_2} = \frac{1}{V_{\Delta_2}} \int G_{\Delta_2} \left\{ \frac{1}{V_{\Delta_1}} \int G_{\Delta_1} a d^3x'' \right\}, d^3x' \tag{71}$$

is equal to one filter step with length scale $\Delta_1 + \Delta_2$, i.e.

$$\left\langle \langle a \rangle^s_{\Delta_1} \right\rangle^s_{\Delta_2} = \langle a \rangle^s_{\Delta_1 + \Delta_2} \, . \tag{72}$$

For $\Delta_1 \to 0$ the first filter would represent a Dirac delta function, that is applicable for a pore size tending to zero, i.e. $D_p \to 0$. Consequently, volume averaged (mean and fluctuating) quantities based on length scale Δ_2 can be obtained by consecutively volume average quantities initially obtained from volume averaging with $\Delta_1 \to 0$ with a filter of length scale Δ_2.

B. MODIFIED WAVE EQUATION

We will verify the proper implementation of the extra terms describing the effect of porosity by comparing simulated results for a plane wave test problem with the analytical solution. For this we consider the simplified case of a medium at rest and a homogeneous porous material that fills out the computational domain. The effect of an anisotropic material is taken into account by considering the matrix μ_{ij} to represent a general symmetric matrix. Based on these prerequisites (i.e. $v_i^0 = 0$, $p^0 = const.$, $\rho^0 = const.$, $\phi = const.$), the pressure and momentum

equation of the linearized Euler equations (as well as Acoustic Perturbation Equation) reduce to

$$\frac{\partial v_i'}{\partial t} + \frac{\phi}{\rho^0}\frac{\partial p'}{\partial x_i} + \mu_{ij} v_j' = 0 \tag{73}$$

$$\frac{\partial p'}{\partial t} + \frac{\gamma p^0}{\phi}\frac{\partial v_i'}{\partial x_i} = 0. \tag{74}$$

We consider the resulting porous wave equation by introducing an acoustic potential that satisfies

$$v_i' = \frac{\partial \varphi}{\partial x_i}. \tag{75}$$

Based on this expressions and using Eq. (74) the time derivatives of pressure and velocity can be expressed via

$$\frac{\partial v_i'}{\partial t} = \frac{\partial^2 \varphi}{\partial t \partial x_i} \tag{76}$$

$$\frac{\partial p'}{\partial t} = -\frac{\gamma p^0}{\phi}\frac{\partial^2 \varphi}{\partial x_i^2}. \tag{77}$$

By taking the time derivative of Eq. (73) and substituting in this resulting expression all the occurring time derivatives of fluctuating pressure and velocity with the previous expressions, a scalar (wave) equation for the acoustic potential is obtained reading

$$\frac{\partial}{\partial x_i}\left(\frac{\partial^2 \varphi}{\partial t^2} - c_0^2 \frac{\partial^2 \varphi}{\partial x_i^2}\right) + \mu_{ij}\frac{\partial^2 \varphi}{\partial t \partial x_j} = 0. \tag{78}$$

Note, the first term in brackets alone represents the wave equation for a medium at rest. The speed of sound[3] in the free fluid[4] resulting therein is obtained from the mean-flow variables as usual as $c_0 = \sqrt{\gamma p^0/\rho^0}$. It is $\gamma = 1.4$ the isentropic exponent of ambient air. The additional term represents the effect of the porosity. To solve this equation system we use coordinates aligned with the main axis of the porosity matrix μ_{ij}.

For this we apply a Galelian transformation to the previous equation using the transformation rules $\partial/\partial t \to \partial/\partial t'$ and $\partial/\partial x_i \to \partial/\partial x_i'$. In the new coordinate system the porosity matrix is diagonal with the diagonal elements prescribed by the corresponding eigenvalues λ_i of μ_{ij}, i.e. $\mu_{ij} \to \mu_{ij}' = \mathrm{diag}(\lambda_i)$ and $\mu_{ij}'\,\partial/\partial x_j' = \lambda_i\,\partial/\partial x_i'$. Hence, in the rotated coordinate system the equation becomes

$$\frac{\partial}{\partial x_i'}\left(\frac{\partial^2 \varphi}{\partial t'^2} - c_0^2 \frac{\partial^2 \varphi}{\partial x_i'^2}\right) + \lambda_i\frac{\partial^2 \varphi}{\partial t' \partial x_i'} = 0. \tag{79}$$

Eventually we make the ansatz to describe the acoustic potential as a superposition of n contributions (in n-D) corresponding to each coordinate direction in the main axis system. For example, in 2-D, the acoustic potential is specified via

$$\varphi(x_1', x_2', t') = \varphi_1(x_1', t') + \varphi_2(x_2', t'). \tag{80}$$

[3]Due to almost constant perturbation variables within the characteristic filter volume—even across an interface between fluid and the porous medium—the Favre fluctuation of the speed of sound vanishes, i.e. $\left[c_0^2\right]'' \to 0$. It finally is $p' = c_0^2 \rho'$.

[4]The sound propagation in the porous material is dispersive, i.e. the phase and the group velocity differ. Please see below

Introducing this ansatz into Eq. (79) we obtain (in 2-D) two independent acoustic equations with individual damping term for each contribution to the acoustic potential, viz.

$$\frac{\partial^2 \varphi_i}{\partial t'^2} - c_0^2 \frac{\partial^2 \varphi_i}{\partial x_j'^2} + \lambda_{(i)} \frac{\partial \varphi_i}{\partial t'} = 0. \tag{81}$$

Note, indices with round brackets indicate suppression of the summation-over-equal-indices rule. Further note, whereas the acoustic particle velocity can be deduced directly by means of Eq. (75) from the acoustic potential, the pressure fluctuations is related to the acoustic potential via Eq. (73). In the main axis system, the relationship(in 2-D) becomes

$$p' = -\frac{\rho^0}{\phi} \left(\frac{\partial \varphi_1}{\partial t} + \lambda_1 \varphi_1 + \frac{\partial \varphi_2}{\partial t} + \lambda_2 \varphi_2 \right) \quad . \tag{82}$$

If we consider harmonic signals with $\hat{\varphi}_j(x_j, t) = \hat{A}_j \exp\left(i\left(\omega t - k_{(j)} x_j\right)\right)$, the corresponding pressure fluctuations reads

$$\hat{p} = -\frac{\rho^0}{\phi} \left[\left(i\omega + \lambda_1\right) \hat{\varphi}_1 + \left(i\omega + \lambda_2\right) \hat{\varphi}_2 \right] \quad . \tag{83}$$

Furthermore, by introducing the harmonic ansatz into the wave-equations we obtain the dispersion relations

$$-\omega^2 + k_j^2 c_0^2 + i\omega\lambda_j = 0. \tag{84}$$

By means of the dispersion relations, the wave number k can be expressed as a function of angular frequency ω,

$$k_j = \frac{\omega}{c_0} \sqrt{1 - i\,\frac{\lambda_j}{\omega}}, \tag{85}$$

yielding the damped wave results

$$\hat{\varphi}_j = \hat{A}_j \exp\left(i\omega \left(t - \frac{1}{c_0} \sqrt{\frac{1}{2} \left[\sqrt{\frac{\lambda_j^2}{\omega^2} + 1} + 1 \right]}\, x_j \right) \right) \exp\left(-\frac{\omega}{c_0} \sqrt{\frac{1}{2} \left[\sqrt{\frac{\lambda_j^2}{\omega^2} + 1} - 1 \right]}\, x_j \right) \tag{86}$$